ELECTRO-STERIC MECHANISM OF CLC-2 CHLORIDE CHANNEL ACTIVATION

José J. De Jesús-Pérez[1], G. Arlette Méndez-Maldonado[2], Irma L. Gonzalez-Hernandez[2], Victor De la Rosa[3], Roberto Gastélum-Garibaldi[2], Jorge E. Sánchez-Rodríguez[2], and Jorge Arreola[1,*]

[1]Physics Institute, Universidad Autónoma de San Luis Potosí, Ave. Dr. Manuel Nava #6, San Luis Potosí, SLP 78290, México.

[2] Departamento de Física, Centro Universitario de Ciencias Exactas e Ingenierías, Universidad de Guadalajara. Blvd. M. García Barragán #1421, Guadalajara, Jal 44430, México.

[3]Cátedra CONACYT, School of Medicine of Universidad Autónoma de San Luis Potosí. Ave. V. Carranza 2005, Los Filtros San Luis Potosí, SLP 78290, SLP, México.

Running Title: Mechanism of CLC-2 gating

Corresponding Author:

*Dr. Jorge Arreola
Instituto de Física, Universidad Autónoma de San Luis Potosí
Dr. Manuel Nava #6
San Luis Potosí, SLP 78290, México
Tel. (444) 826-2363 ext 136
Fax (444) 813-3874
Email: arreola@dec1.ifisica.uaslp.mx

ABSTRACT

Two-pore voltage-gated CLC chloride channels control neuronal and muscle excitability. They share a dimeric structure but their activation mechanism remains unresolved. Here we determine the step-by-step activation mechanism of the broadly expressed CLC-2 channel using homology modelling, molecular dynamic simulations and functional studies. We establish that a two-leaf gate formed by Tyr561-H_2O-Glu213 flanked by Lys568/Glu174 and Lys212 closes the canonical pore. Activation begins when a hyperpolarization-propelled intracellular chloride occupies the pore and splits Tyr561-H_2O-Glu213 by electrostatic/steric repulsion. Unrestrained Glu213 rotates outwardly to bind Lys212 but the pore remains closed. Protonation breaks the Glu213-Lys212 interaction while another chloride occupies the pore thus catalysing chloride exit via Lys212. Also, we found that the canonical pore is uncoupled from a cytosolic cavity by a Tyr561-containing hydrophobic gate that prevents Glu213 protonation by intracellular protons. Our data provide atomistic details about CLC-2 activation but this mechanism might be common to other CLC channels.

KEYWORDS:

Ion channel gating, CLC chloride channel, ClC-2 gating, pore occupancy, H^+, chloride.

INTRODUCTION

Gating is a fundamental property whereby membrane channels open a permeation pathway so ions can passively flow in or out of the cells, thus ensuing electric communication(Bezanilla, 2008; Hille et al., 1999; Jiang et al., 2003; Long et al., 2005). In some channels, a sudden change in the membrane electrical field, ligand binding or lipid bilayer forces triggers a cascade of structural rearrangements that ultimately open the permeation pathway(Bezanilla, 2008, 2002; Cox et al., 2016; Goldschen-Ohm and Chanda, 2017; Hille et al., 1999; Jiang et al., 2003; Long et al., 2005). CLC chloride (Cl^-) channels are voltage-activated or type III(Goldschen-Ohm and Chanda, 2017) channels despite lacking a canonical voltage sensor(Jentsch and Pusch, 2018), however, the molecular mechanism of voltage-dependent activation remains elusive.

The CLC protein family includes Cl^- channels (CLC-0, CLC-1, CLC-2, CLC-Ka, and CLC-Kb) and 2:1 Cl^-/H^+ exchangers that are structurally conserved(Jentsch and Pusch, 2018). They share a double pore architecture, each pore is closed by a highly conserved Glu residue called Glu_{gate} that protrudes into the permeation pathway(Dutzler et al., 2003, 2002; Park et al., 2017; Park and MacKinnon, 2018). This structure of the pore suggested that voltage gating may occur unconventionally(Schewe et al., 2016). Glu_{gate} would be open by repulsion when voltage drives a permeant anion into the pore(Chen, 2003; De Jesús-Pérez et al., 2016; Pusch et al., 1995; Sánchez-Rodríguez et al., 2012, 2010) and/or by protonation when voltage drives a proton into the pore(Niemeyer et al., 2009a; Traverso et al., 2006a). Data collected varying the extracellular anion concentration or the anion mole fraction supported the idea that CLC-0 and CLC-1 channels were gated by permeant anions repelling the Glu_{gate}(Chen, 2003; Pusch et al., 1995;

Rychkov et al., 1998, 1996). However, data collected under acidic cytosolic conditions led to an alternative gating mechanism in CLC-0. This alternative mechanism invokes voltage-dependent protonation of Glu_{gate} by intracellular protons(Miller, 2006; Traverso et al., 2006a), a reaction catalysed by extracellular Cl^- anions(Miller, 2006). Although this hypothesis may explain CLC-0 and CLC-1 gating, the gating of CLC-2 diverges from this. CLC-2 activation depends on hyperpolarization and intracellular Cl^- while depolarization causes deactivation(De Santiago et al., 2005; Sánchez-Rodríguez et al., 2010; Thiemann et al., 1992). Furthermore, anions unable to permeate the pore when applied from the intracellular side still support CLC-2 voltage gating(De Jesús-Pérez et al., 2016). Notable, intracellular acidification has little effect on gating. In contrast, extracellular acidification increases the apparent open probability(Niemeyer et al., 2009b) in a voltage-independent manner(Sánchez-Rodríguez et al., 2012) but CLC-2 is still activated under unfavourable protonation condition ($[H^+]_e$ = 10^{-10} M)(De Jesús-Pérez et al., 2016). Thus, protonation cannot explain voltage-dependent activation. Instead, we proposed that hyperpolarization drives Cl^- into the pore causing Glu_{gate} to be open by electrostatic and steric repulsion(De Jesús-Pérez et al., 2016; Sánchez-Rodríguez et al., 2010) and then CLC-2 Glu_{gate} protonation stabilizes its open conformation(Sánchez-Rodríguez et al., 2012).

Establishing an activation mechanism for CLC Cl^- channels has been hindered by limited structural information on these channels and the challenge that impose gathering information about a process that occurs in nanosecond time scale within a narrow pore. Here we combined quantitative functional analysis with molecular dynamics (MD) simulations to overcome these limitations and to establish the molecular mechanism of CLC-2 activation, a Cl^- channel highly

89 expressed throughout the central nervous system that controls neuronal excitability and
90 aldosterone secretion(Boccaccio et al., 2018; Jentsch and Pusch, 2018; Thiemann et al., 1992).

91 **RESULTS**

92 **A water-mediated Tyr561-Glu$_{gate}$ ionic interaction holds the CLC-2 pores closed.**

93 To study CLC-2 activation, CLC-2^{CLC-K} and CLC-2^{CLC-1} homology models of the CLC-2 structure
94 were built using the CLC-K (5TQQ)(Park et al., 2017) and hCLC-1 (6COY)(Park and MacKinnon,
95 2018) Cl^- channel structures as templates. Both CLC-2^{CLC-K} and CLC-2^{CLC-1} are dimers with a
96 transmembrane domain (TMD) comprising 17 α-helices termed B-R (Fig. 1A). Helix A (residues 1
97 to 96), which is not in the template structures, next to the N-terminus could not be modelled.
98 Only the CLC-2^{CLC-K} structure included the C-terminus with two cystathionine-β-synthase (CBS)
99 domains. Both models show the classical rhombus shape of the CLC protein structures when
100 viewed from the top. The root mean square deviation between TMD backbones of these models
101 is 1.0 Å and becomes 3.0 Å after adding the C-terminus.

102

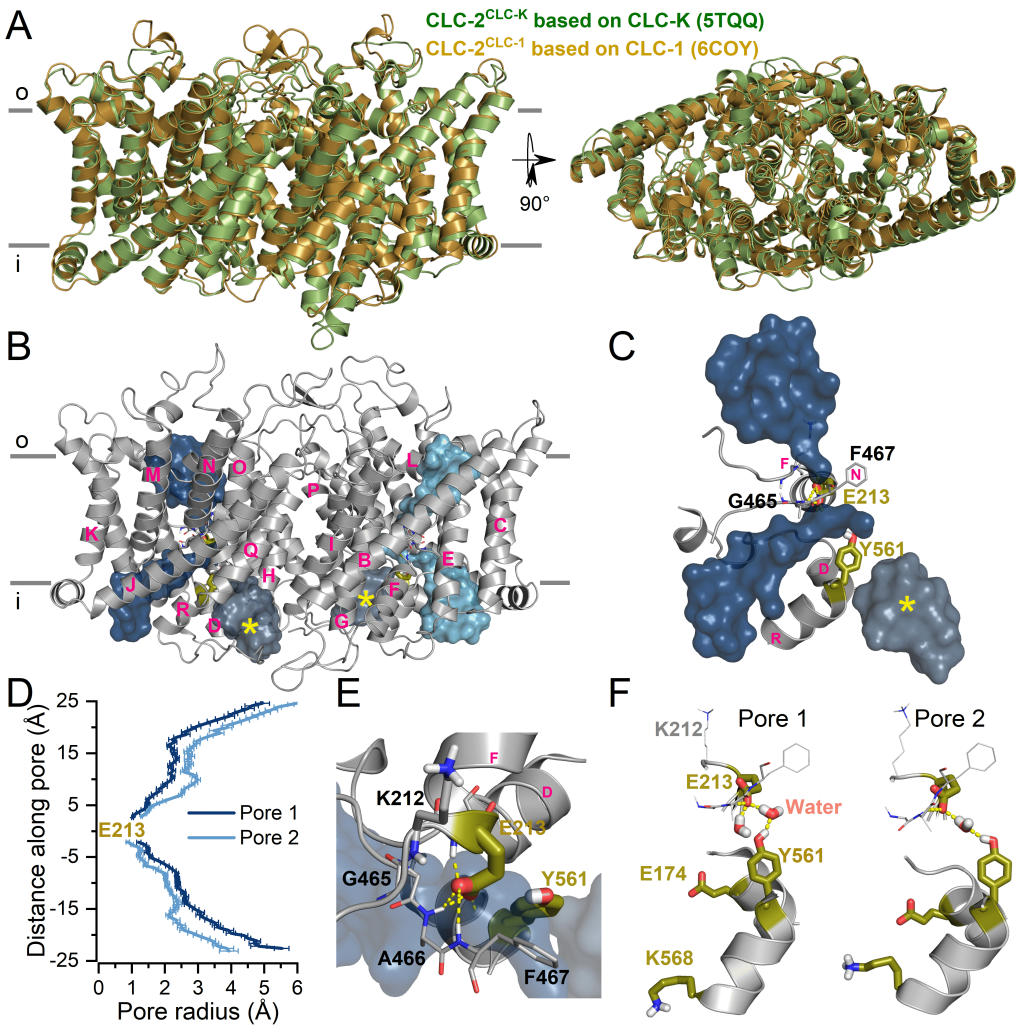

Fig. 1 Homology models of the CLC-2 structure.

A. Homodimeric models based on the cryo-EM structure of CLC-K (5TQQ, green) and hCLC-1 (6COY, orange) channels showing a view of the transmembrane domains from the membrane plane (left) or the top (right). Parallel grey lines indicate external (o) and internal (i) membrane limits. Both structures are similar (RMSD = 1.0 Å). For clarity, the intracellular carboxyl tail containing the CBS domains was not included.

B. CLC-2 homology model based on the hCLC-1 structure after 30 ns of MD simulation. The names of the transmembrane helixes are shown in pink letters (B-R). The canonical pores

flooded with water are represented as dark and light blue surfaces in each subunit. The intracellular alternative pathways are shown in grey marked with yellow asterisks.

C. *The canonical pore (dark blue) and the intracellular alternative pathway (yellow asterisk) within one subunit of CLC-2. Water molecules filling these cavities represent the structure. Tyr561 and Glu213 (Glu_{gate}) are shown in olive. Note that Tyr561 separates the canonical pore and the intracellular aqueous pathway. Glu_{gate} is located at the centre of the canonical pore where the water chain is interrupted.*

D. *Average pore radius along canonical pores. The radius was measured using CAVER*(Chovancova et al., 2012) *every 1 ns during 30 ns at 0 mV. Deep and light blue colours correspond to pores 1 and 2 shown in panel B.*

E. *Close-up showing stabilization of Glu_{gate} by interactions with residues $_{465}GAF_{567}$ and Lys212 (sticks).*

The CLC-2 gate is formed by Tyr561-H_2O-Glu_{gate}. Hydrogen bonds (dashed yellow lines) link Glu_{gate} to Tyr561 through one (right) or two (left) water molecules (ball and stick representation). Additionally, residues Lys568 and Glu174 on the intracellular side and Lys212 on the extracellular side are shown.

To determine the radius and shape of the pore, CLC-$2^{CLC\text{-}K}$ and CLC-$2^{CLC\text{-}1}$ were embedded in DMPC and POPC bilayers, hydrated with 140 mM NaCl and equilibrated using the CHARMM-GUI protocol(Allouche, 2012) at 0 mV during 100 ns and 30 ns, respectively. The initial position of Glu_{gate} in each model was different but reached the same position after equilibration (Supplementary Fig. 1). The canonical CLC-2 pore is formed by residues $_{164}$APQAVGSGIPEM$_{175}$,

$_{209}$PLGKEG$_{214}$, $_{458}$TTIPVPCGAFMP$_{469}$, and $_{561}$YDSIIRIK$_{568}$ located at the N-termini of αD, αF, αN, and αR helices (Fig. 1B), respectively. Lys212 and Lys568 + Glu174 were located at the extracellular and intracellular entrances, respectively (Fig. 1E and 1F). Each monomer has a curvilinear permeation pathway filled with water and disrupted at the centre by Glu213 (Glu_{gate}) (Fig. 1C). At each end of these canonical pores, there is a large water cavity. A third water cavity resembling the bifurcated pathway of hCLC-1(Park and MacKinnon, 2018) was observed in the cytosolic side (Fig. 1C, yellow star). However, this cavity is uncoupled from the canonical pore by bulky Tyr561. The radius of the pore in each monomer is shown in Fig. 1B (dark and light blue); each pore is less than 0.5 Å at the side chain of Glu_{gate} (Fig. 1D). Thereafter, the radius increases to about 2.5 Å at ± 15 Å away from Glu_{gate} and even more at both pore entrances. At 0 mV, the charged carboxyl group of Glu_{gate} is stabilized by hydrogen bonds (H-bonds) with the amino groups of $_{466}$AF$_{467}$ and $_{212}$KEG$_{214}$ (Fig. 1E). Also, Glu_{gate} forms an ionic interaction with the –OH group of Tyr561 via H-bonds mediated by one H_2O molecule (Fig. 1F). This conformation is similar to that of Glu_{gate} in CmCLC and in rCLC-2 models built using the CmCLC structure(Feng et al., 2010; McKiernan et al., 2020). We propose that the Tyr561-H_2O-Glu_{gate} array forms the gate that maintains CLC-2 in the closed state.

Gating is a multistep process triggered by Cl^-.

To investigate the conformational changes that lead to CLC-2 opening we performed MD simulations using CLC-2^{CLC-K} and the three compartments/two-bilayer computational electrophysiology method (CompEl)(Kutzner et al., 2011). Each bilayer containing one channel was simultaneously exposed to the same voltage but opposite polarity during 480 ns ($^{+}$CLC-2^{CLC-K}

in bilayer 1 to +94 and +940 mV and $^{-}$CLC-2$^{CLC\text{-}K}$ in bilayer 2 to -94 and -940 mV). This protocol was followed by applying a uniform electric field(Crozier et al., 2001; Roux, 2008) of -500 mV perpendicular to bilayer 2 during 200 ns.

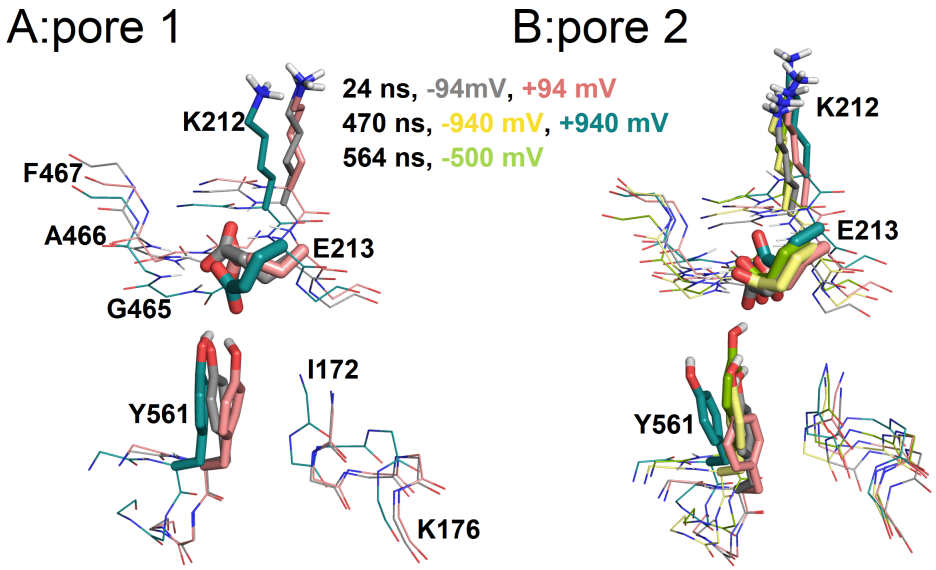

Fig. 2 Changes in the transmembrane voltage do not trigger gating when the pores are empty.

The conformation of three pores: pore 1 of $^{+}$CLC-2$^{CLC\text{-}K}$ (A) and pore 2 of $^{-}$CLC-2$^{CLC\text{-}K}$ and $^{+}$CLC-2$^{CLC\text{-}K}$ (B) channels are depicted at different voltages (-94, -940, 500, +94, and +940 mV) and MD simulation times (24, 470, and 564 ns). The spatial position of Tyr561, Glu$_{gate}$, and Lys212 is shown. Note that Glu$_{gate}$ remained at the same position regardless of the transmembrane voltage.

First, we determined whether the closed Glu$_{gate}$ position was altered by hyperpolarization or depolarization in Cl^{-}-free pores (pore 2 of $^{-}$CLC-2$^{CLC\text{-}K}$ and pores 1 and 2 of $^{+}$CLC-2$^{CLC\text{-}K}$). Relative to 0 mV, we observed little o no changes in the position of Tyr561, Glu$_{gate}$, and Lys212 at positive

or negative voltages (Fig. 2). Regardless of voltage, Glu_{gate} was stabilized by H-bonds formed at different times with either the -OH group of Tyr561 via one H_2O molecule (97% of the total simulation time; lifetime 63-116 ps) or with -NH group of residues $_{466}AF_{467}$ and $_{212}KEG_{214}$ (3%, lifetime 2.9-4.4 ps), and by direct interaction with Tyr561 (0.12%). When a +940 mV was applied to $^{+}CLC\text{-}2^{CLC\text{-}K}$, the Glu_{gate} in pore 1 was pushed inwardly and displaced the water molecule that bridges Tyr561 and Glu_{gate} (Fig. 2A, cyan). This displacement increased the Tyr561-Glu_{gate} direct interaction to 40%. Thus, voltage alone cannot open the CLC-2 gate.

Second, we examined the structural rearrangements that residues lining pore 1 of $^{-}CLC\text{-}2^{CLC\text{-}K}$ underwent at negative voltage when five Cl^- ions occupied the pore (Cl^-1-Cl^-5). Based on the time (≥ 1 ns) that a Cl^- ion spent on sections along the pore, we defined four putative binding sites: intracellular S_i formed by Lys568 and Glu174, central S_c formed by Tyr561 and Ile172, external S_e formed by $_{465}GlyAlaPhe_{467}$, and exit S_o formed by Lys212 and Glu213. Figure 3A shows snapshots of pore 1 of $^{-}CLC\text{-}2^{CLC\text{-}K}$ at 0, 24, 37, 470, 513, 526, 541, 564, 579, 605, 654, and 663 ns into the MD simulation (arrowheads in the site occupation roster, right side of Fig. 3B). The snapshots depict the journey of Cl^-3 through the entire pore in five steps:

Pore occupation. Figure 3A (snapshot at 0 ns and -94 mV) shows pore residues and 8 water molecules to indicate an empty permeation pathway closed by Tyr561-H_2O-Glu_{gate} gate. The side chains of Lys568 and Glu174 fluctuated between 2-5 Å. Figure 3B shows that Cl^-1 and Cl^-2 occupied S_i for 11.5 and 3.4 ns and then spontaneously returned to the intracellular side. As Cl^- ions visited the pore, the side chains of Lys568 and Glu174 became closer (2 Å). Then Cl^-3 occupied S_i during 3.5 ns (Figs. 3A and 3B, snapshot at 24 ns).

Disruption of Tyr561-H_2O-Glu_{gate}. Cl^-3 moved to S_c (snapshot at 37 ns) disrupting the water bridge between Tyr561 and Glu_{gate} and binding to Tyr561. The electrostatic and steric forces (or electro-steric forces) repelled Glu_{gate} outwardly. Subsequently, Glu_{gate} interacted with the Lys212 side chain and the $_{213}EG_{214}$ backbone. Unlike in the empty pore, now Glu_{gate} stopped interacting with Gly214, folded in itself and remained attached to its backbone 59% of the time (lifetime 12.5 ps). Simultaneously, the number of H-bonds between Glu_{gate} and Lys212 increased from 1 to 3 during 98.8% of the simulated time (CompEl protocol; lifetime 274 ps). To accelerate the permeation process, we increased the voltage from -94 to -940 mV at t = 145 ns and this stabilized Cl^-3 at S_e (Fig. 3B; snapshot at 470 ns). The majority of the time Cl^-3 dwelt between S_c (133 ns) and S_e (320 ns) (Fig. 3B) and S_e became closer to S_o because $_{212}LysGlu_{gate}$ adopted an intermediate position between the closed and open configurations (Supplementary Fig. 2A).

Glu_{gate} protonation. We had reported that Glu_{gate} is stabilized in the open conformation by extracellular H^+ in a voltage-independent manner(Sánchez-Rodríguez et al., 2012). Hence, we asked whether protonation was necessary to disentangle Glu_{gate} from S_e. At t = 484 ns (Fig. 3A), the carboxyl group of Glu_{gate} was protonated using CHARMM-GUI. After protonation (snapshot at t = 513), the H-bond between Glu_{gate} and Lys212 was lost; Cl^-3 stayed for 10.5 ns on S_e and then occupied S_o (snapshot at 526 ns).

Multi-ion pore occupancy. After disengaging Glu_{gate} from Lys212, Cl^-4 entered and interacted with S_i for 22 ns (snapshot at 526 ns). Then Cl^-4 jumps (snapshot at 541 ns) and fluctuates between S_c (for 14.4 ns) and S_e (57.1 ns). The hop of Cl^-4 into S_c tilts Lys212 counter-clockwise by about 45° without altering Glu_{gate}.

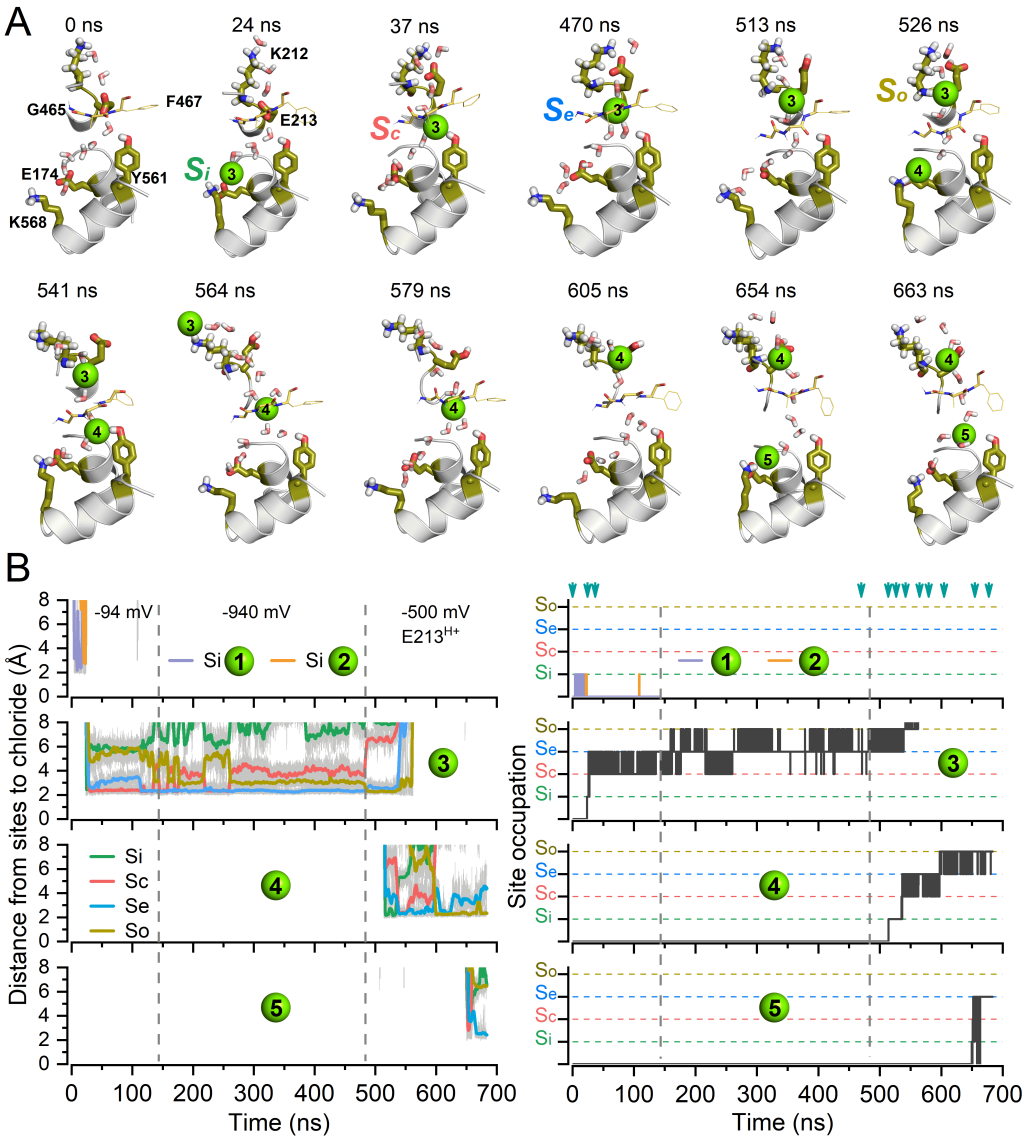

210

211 ***Fig. 3 Coupling gating to permeation enables CLC-2 activation at the molecular level.***

212 *A. Snapshots of structural rearrangements of key residues located in pore 1 of* $^{-}$*CLC-2*$^{CLC\text{-}K}$

213 *channel sampled by MD simulation at the times indicated on top of each structure. Ball and*

214 *stick representation of Lys568, Glu174, Tyr561, Glu213, Gly465, Ala466, Phe467, and Lys212*

215 *along with eight water molecules illustrate the canonical permeation pathway (snapshots at*

216 *0 and 24 ns). Green spheres represent* Cl^{-} *ions. Hyperpolarisations applied were -94, -940,*

and -500 mV. Snapshots are representative of pore occupation (24 ns), displacement of Glu_{gate} (37 and 470 ns), Glu_{gate} protonation (513 ns), double occupancy (526 and 541 ns) and exit of Cl^- from the pore (564 and 579 ns). Snapshots at 605, 654, and 663 ns illustrate changes in permeation caused by double occupancy. Residues participating in Cl^- transport and gating (Glu174, Lys568, Tyr561, Glu213, and Lys212) are shown in olive. The internal (Lys568-Glu174, green), centre (Tyr561, pink), external ($_{465}$GAF$_{467}$, blue), and extracellular ($_{212}$KGlu$_{213}$, olive) sites that are occupied by Cl^- along the pore are labelled as S_i, S_c, S_e, and S_o, respectively.

B. Left: The distance separating Cl^- from the binding sites (S_i, S_c, S_e, and S_o) is shown as a function of the simulation time. Right: Site occupation determined by the time spent by Cl^- at each binding site during the simulation. Five Cl^- ions visited the intracellular side of the pore during the entire 680 ns MD simulation. Of these, only Cl^-3, Cl^-4 and Cl^-5 occupied the pore. Cl^-1 (lavender) and Cl^-2 (light green) at the top, next Cl^-3, then Cl^-4, and Cl^-5 at the bottom. Dashed vertical lines indicate the time when the transmembrane voltage was changed from -94 to -940 mV and from 940 to -500 mV. -94 and -940 mV was applied using CompEl. -500 mV was applied using an electric field after Glu213 was protonated ($E213^{H+}$). Cyan arrowheads on the top (right panel) indicate times at which the snapshots shown in A were captured.

Pore exit. Further outward movement of Cl^-4 near S_o induced straightening of Lys212 and placed Cl^-3 onto the Lys212 side chain end for 66.7 ns (Fig. 3A, snapshot at 564 ns). The total conformational change translated the $_{212}$KEG$_{214}$ backbone ~6 Å away from the closed position

(Supplementary Fig. 2B and Fig. 2C). The lengthy interaction of Cl^-3 with S_o could be explained by an enhancement of the electrostatic potential at Lys212 position in the open state (Supplementary Fig. 3). Finally, Cl^-3 escapes the pore (snapshot at t = 579 ns) ending its 580 ns journey while Cl^-4 sits onto S_o for 76 ns (snapshot at t = 605 ns). At this time, Cl^-5 occupies S_i (for 1.1 ns, snapshot at 654 ns), then S_c (for 4.5 ns, t = 663 ns), and S_e (for 27.4 ns) signalling that the pore is fully open/conductive and that Cl^-4 is near to exit the pore.

These steps, stitched in the video, agree with previous results emphasizing that CLC-2 gating requires intracellular Cl^-, protonation by external H^+, and multi-ion occupancy(De Jesús-Pérez et al., 2016; Sánchez-Rodríguez et al., 2012, 2010).

Video: 1 CLC-2 Activation mechanism

Trajectory of Cl^-3 along the pore at -94 mV (0-47 ns) and after protonation of Glu_{gate} at -500 mV (485-660 ns). Pore 1 of $^-CLC\text{-}2^{CLC\text{-}K}$ is shown. Membrane surface profile (phosphates) is represented by grey spheres. Lys568, Glu174, Tyr561, Glu213, Gly465, Ala466, Phe467, and Lys212 are represented in olive sticks, Cl^- in green spheres, and helix in white. Top side = extracellular side; lower side = intracellular side.

Tyr561-H_2O-Glu_{gate} array controls gating.

Earlier studies with CLC-0 and CLC-1 carrying a Tyr mutation in the pore showed no change in conductance between WT and mutant channels(Accardi and Pusch, 2003; Estévez et al., 2003; Ludewig et al., 1996). Those studies led to the conclusion that Tyr561 plays no role in CLC-2 gating(McKiernan et al., 2020). However, our MD simulations show otherwise. We revealed the

role of Tyr561 by mutagenesis and functional studies. The activity of Tyr561Phe, Tyr561Ala and Glu213Asp mutant channels was determined using both patch-clamp and cut-open oocyte voltage-clamp techniques. The Tyr561Ala mutant channel shows currents in both directions revealing an open channel phenotype (Fig. 4A) while WT and Tyr561Phe channels displayed currents with similar kinetics. Similarly, we reasoned that the Tyr561-H_2O-Asp213 array in the Glu213Asp mutant loses stability and mimics the gating behaviour of Tyr561Ala. Indeed, positive voltages activate the Glu213Asp channel but negative voltages induce currents similar to those of WT; tail currents were smaller and faster.

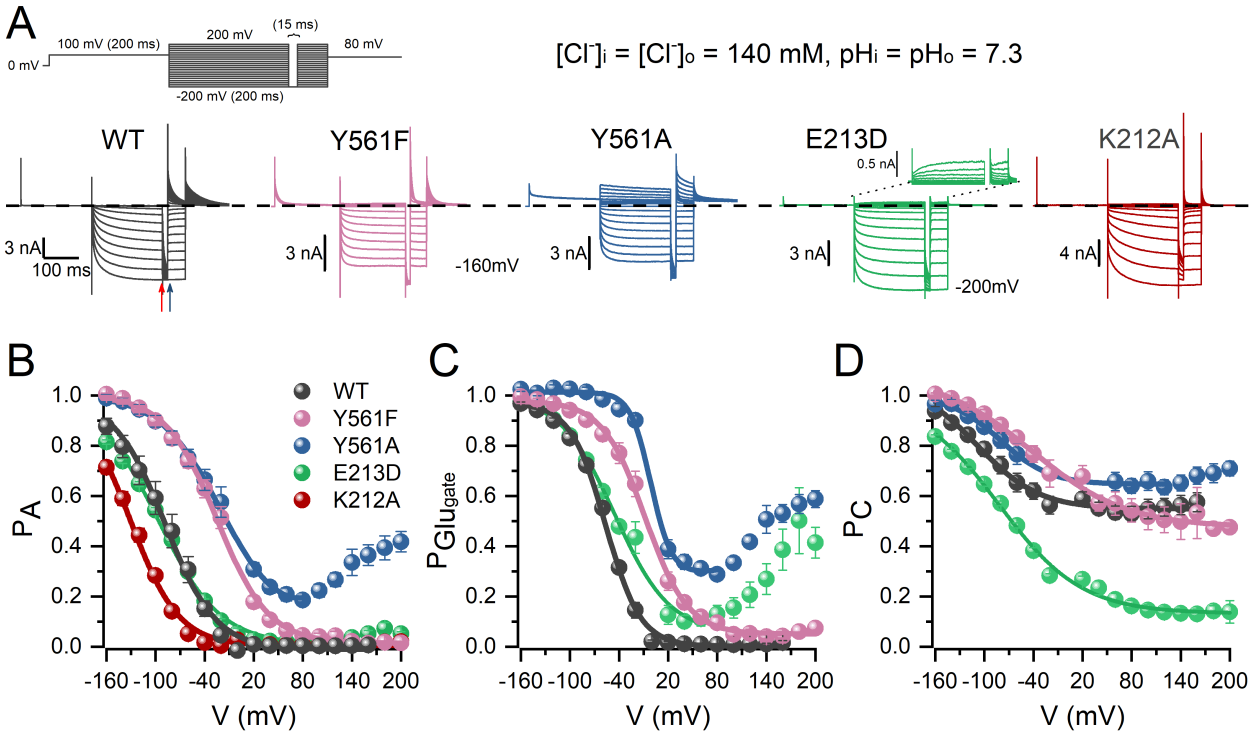

Fig. 4 Tyr561 and Glu213 control voltage-dependent activation.

A. Cl^- currents (colour-coded) recorded from 5 different HEK293 cells expressing WT CLC-2 (WT), Tyr561Phe (Y561F), Tyr561Ala (Y561A), Glu213Asp (E213D), and Lys212Ala (K212A). Cl^-

currents were elicited by the voltage protocol shown in the upper panel. The protocol consisted in depolarization steps from -200 to 200 mV in 20 mV increments; we introduced an inter-pulse of 15 ms at -200 mV to reach $P_{Glugate}$ = 1 and a repolarization voltage to +80 mV to record tail currents. Cl^- currents were acquired using $pH_i = pH_o = 7.3$ and $[Cl^-]_i = [Cl^-]_o$ = 140 mM. Dash line indicates $I_{Cl} = 0$.

B. *Apparent open probability (P_A) computed for WT CLC-2, Tyr561Phe, Tyr561Ala, Glu213Asp, and Lys212Ala. Continuous lines represent data fitted with the Boltzmann equation to determine voltage-dependent parameters $V_{0.5}$ and z, listed in Table 1.*

C. *,D. Voltage dependence of Glu_{gate} ($P_{Glugate}$) and common gate (P_C) obtained for WT CLC-2, Tyr561Phe, Tyr561Ala, Glu213Asp, and Lys212Ala. The probability of each gate was calculated as described in the methods section. Continue lines are fits to Boltzmann equation to determine the voltage-dependent parameters ($V_{0.5}$ and z) listed in Table 1.*

Values for the parameters ($V_{0.5}$ and z) describing the voltage dependence of apparent open probability (P_A), Glu_{gate} open probability ($P_{Glugate}$), and common gate open probability (P_C)(De Santiago et al., 2005) (Figs. 4B, 4C, and 4D) are summarized in Table 1. The $V_{0.5}$ (mV)/z values for P_A, of WT and Glu213Asp channels were quite similar: -89.3 ± 8.5/-0.84 ± 0.04 and -97.8 ± 3.3 /-0.64 ± 0.01, respectively. In contrast, the $V_{0.5}$ values for both Tyr561Phe and Tyr561Ala mutants displayed a large rightward shift without changing z (Fig. 4B, Table 1). The changes mainly involved $P_{Glugate}$ $V_{0.5}$ values (Fig. 4C). For Tyr561Phe and Tyr561Ala, the $P_{Glugate}$ $V_{0.5}$ values were rightward shifted by ~+50 mV relative to WT $P_{Glugate}$ (-56.6±1.0 mV). Notable, although both Glu213Asp and Tyr561Ala displayed reopening of "Glu_{gate}" at positive voltages, the $V_{0.5}$ value for Glu213Asp was similar to that of WT. Overall, the voltage dependence of P_C (Fig. 4D) seems to

be quite similar in WT, Tyr561Phe, and Tyr561Ala. However, the voltage dependence of P_C in Glu213Asp indicates that the common gate starts to close at voltages that are more negative and is fully closed at positive voltages. These results indicate that Tyr561 keeps Glu_{gate} closed; a conclusion further supported by WT, Tyr561Phe, and Tyr561Ala data collected using the cut-open oocyte technique (Supplementary Fig. 4 and Table 1).

Channel	$V_{0.5}^{P_A}$ (mV)	z_{P_A}	$V_{0.5}^{P_P}$(mV)	z_{P_P}	$V_{0.5}^{P_C}$ (mV)	z_{P_C}	Er (mV)	pH_i	$[Cl^-]_o$ (mM)	n
WT-HEK	*-89.3 ± 8.5*	*-0.84 ± 0.04*	*-56.6 ± 1.0*	*-1.17 ± 0.07*	*-110.9 ± 6.3*	*-0.75 ± 0.03*		*7.3*	*140*	*5*
WT-OOC	-96.9 ± 7.5	-0.87 ± 0.04	-72.3 ± 1.4	-1.24 ± 0.10	-115.1 ± 5.5	-1.17 ± 0.13		7.3	140	7
WT	-79.1 ± 5.8	-0.79 ± 0.07	-39.5 ± 2.2	-1.19 ± 0.07	-82.9 ± 6.1	-0.54 ± 0.04	57.4 ± 0.6	7.3	10	5
Y561F-HEK	*-34.8 ± 9.4*	*-0.8 ± 0.0*	*-13.8 ± 6.4*	*-1.1 ± 0.1*	*-51.2 ± 6.4*	*-0.4 ± 0.0*		*7.3*	*140*	*9*
Y561F-OOC	-29.7 ± 7.6	-0.57 ± 0.05	-5.66 ± 9.9	-0.71 ± 0.05	-37.3 ± 17.9	-0.62 ± 0.1		7.3	140	7
Y561F	-68.9 ± 5.4	-0.67 ± 0.02	-6.3 ± 4.4	-0.73 ± 0.04	-71.9 ± 4.5	-0.62 ± 0.07	52.5 ± 1.6	7.3	10	6
Y561F	-40.0 ± 4.5	-0.77 ± 0.04	-21.6 ± 2.2	-0.95 ± 0.08	-36.1 ± 7.9	-0.53 ± 0.06		5.5	140	8
Y561F	-60.3 ± 17.8	-0.73 ± 0.08	-17.9 ± 8.6	-1.09 ± 0.17	-78.7 ± 23.2	-0.63 ± 0.06		4.3	140	5
Y561A-HEK	*-30.4 ± 5.9*	*-0.84 ± 0.09*	*-4.1 ± 2.5*	*-1.48 ± 0.12*	*-65.6 ± 10.6*	*-0.81 ± 0.06*		*7.3*	*140*	*7*
Y561A-OOC	-37.4 ± 6.1	-0.85 ± 0.04	-41.8 ± 15.2	-1.18 ± 0.08	-64.0 ± 1.88	-1.05 ± 0.01		7.3	140	3
Y561A	-58.6 ± 8.6	-0.63 ± 0.01	25.8 ± 4.7	-1.08 ± 0.06	-74.5 ± 7.3	-0.64 ± 0.07	57.5 ± 0.8	7.3	10	6
Y561A	-31.7 ± 6.5	-0.82 ± 0.07	-13.4 ± 2.6	-1.04 ± 0.08	-77.2 ± 15.9	-0.98 ± 0.16		5.5	140	9
Y561A	-38.6 ± 8.0	-0.89 ± 0.15	-12.7 ± 5.2	-1.26 ± 0.09	-66.7 ± 12.1	-0.77 ± 0.07		4.3	140	10
E213D	-97.8 ± 3.3	-0.64 ± 0.01	-44.6 ± 3.6	-0.82 ± 0.05	-86.0 ± 6.1	-0.51 ± 0.01		7.3	140	8
K212	-130.7 ± 3.6	-1.16 ± 0.03	--	--	--	--	--	7.3	140	6

TABLE 1. Effect of $[H^+]_i$ and $[Cl^-]_O$ on the voltage-dependent parameters of WT and mutants CLC-2 channels. *$V_{0.5}^{P_A}$ = voltage to reach an open probability of 0.5, z_{P_A} = apparent charge of the open-closed transition, $V_{0.5}^{P_P}$ = voltage to reach a 0.5 open probability of Glu_{gate}, z_{P_P} = apparent of Glu_{gate} charge, $V_{0.5}^{P_C}$ = voltage to reach a 0.5 open probability of the common gate, z_{P_C} = apparent charge the common gate. These parameter values were calculated by fitting the data to the Boltzmann equation (Equation 1). Er = reversal potentials determined by current-voltage*

relationship interpolations. HEK = data collected from HEK 293 cells; OOC = data collected from cut-open oocytes.

MD simulations suggest that Lys212 is relevant for Cl^- exit. To confirm the role of Lys212, we first calculated the electrostatic potential in the closed and open pores of WT and $^-$CLC-2$^{CLC\text{-}K}$ Lys212Ala mutant (produced *in silico*). The electrostatic potential decreased from -26 Kcal/mol to -12 Kcal/mol (closed) and from -52 Kcal/mol to -40 Kcal/mol (open) after mutating Lys212 (Supplementary Fig. 3). Then, we determined the voltage dependence of P_A from whole cell recordings of the Lys212Ala mutant channel (Fig. 4A). Mutant channels activated with kinetics similar to that of WT; at -200 mV, the time constants of the fast kinetic component were 3.2 ± 0.7 ms and 3.8 ± 0.5 ms, for the slow component were 41.0 ± 3.9 ms and 40.1 ± 7.9 ms for mutant and WT, respectively. Unlike WT, the mutant channels had very fast closing; at +80 mV, the time constants were 4.7 ± 0.24 ms for mutant and 59.4 ± 4.8 ms for WT. This result indicates that Lys212 helps to keep the pore in the open conformation. In agreement with this idea, the voltage dependence of P_A in the Lys212Ala mutant channel (Fig 4B; Table 1) was shifted to negative voltages ($V_{0.5}/z$ = -130.7±3.6 mV/1.16±0.03).

WT CLC-2 has low sensitivity to extracellular $[Cl^-]$ ($[Cl^-]_o$)(Sánchez-Rodríguez et al., 2010). However, Glu_{gate} could become sensitive to $[Cl^-]_o$ when is dislodged, as in the Tyr561Ala mutant (Fig. 4). The Cl^- influx in Tyr561 mutants would knock off Glu_{gate} inwardly just as the Cl^- efflux knocks off the WT Glu_{gate} outwardly. Under whole cell condition, the $[Cl^-]_o$ was changed from 140 to 10 mM, this manoeuvre decreased Cl^- influx but had little effect on the kinetics of WT, Ty561Phe, and Tyr561Ala currents (Fig. 5A, 5B and 5C). The voltage dependence of P_A and $P_{Glugate}$ in the WT channel was little or not affected by varying the $[Cl^-]_o$ (Fig. 5A, Table 1).

However, in Tyr561Phe channels (Fig. 5B), we observed a -34 mV shift on $V_{0.5}$ of P_A with little effect on $P_{Glugate}$ (Table 1). A severe alteration of the voltage dependence of both P_A and $P_{Glugate}$ was observed in the Tyr561Ala mutant at positive voltages (Fig. 5C). In this mutant, the voltage dependence of P_A was shifted by about -29 mV and re-opening at positive voltages was abolished by lowering the $[Cl^-]_o$ from 140 to 10 mM. Similarly, $P_{Glugate}$ was strongly diminished at positive voltages. That is, decreasing the Cl^- influx decreased the open probability of Glu_{gate} at positive potentials in the Tyr561Ala mutant channel. In contrast, the effect of low $[Cl^-]_o$ on $V_{0.5}$ of P_C was nearly the same in WT, Tyr561Phe and Tyr561Ala channels ($V_{0.5}$ were between -71 to -82 mV, Table 1). The common gate tended to close at low external Cl^- conditions.

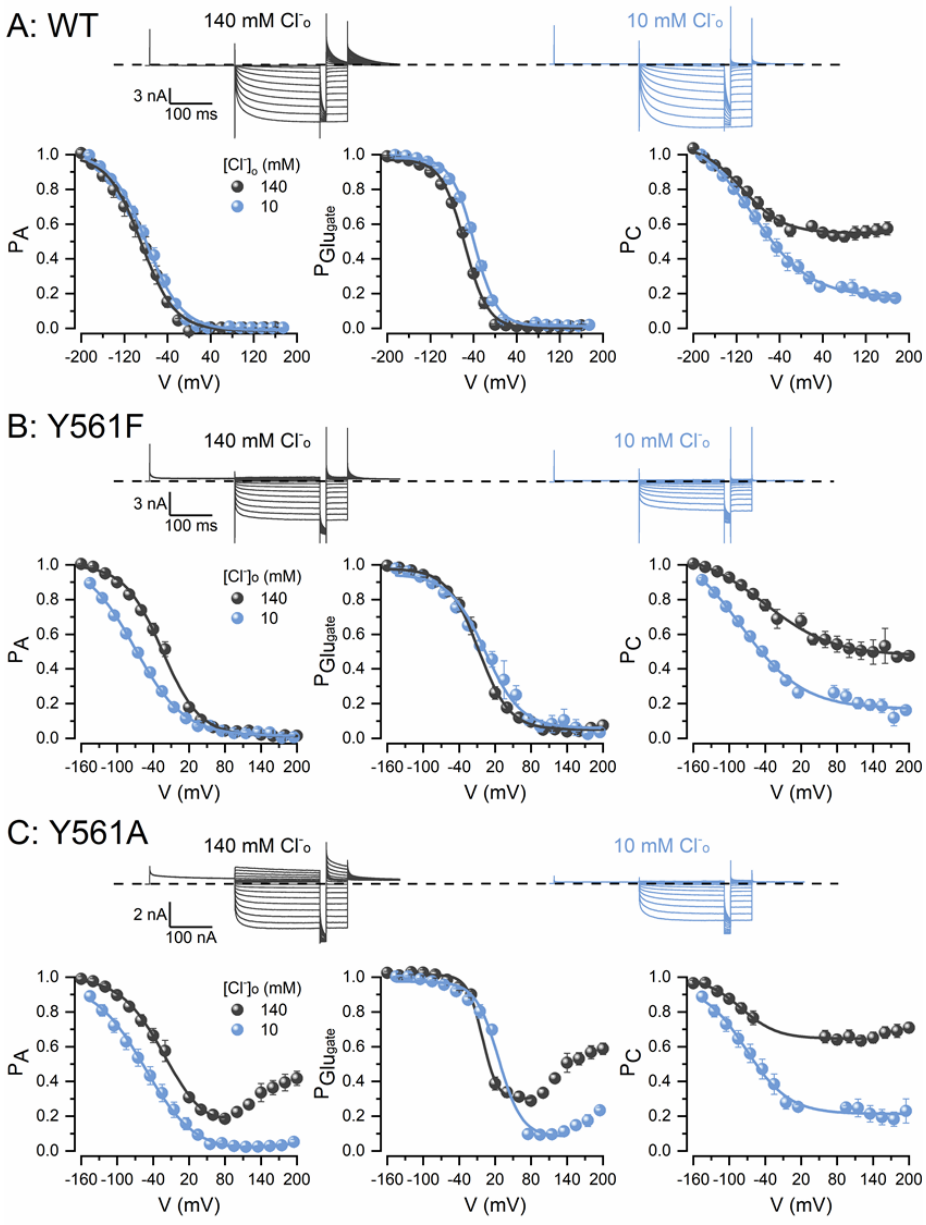

Fig. 5 TMEM16A channels that have Tyr561 mutated to Phe or Ala are sensitive to extracellular chloride.

A,B,C. Top panels: Cl^- currents recorded from the same HEK293 cell expressing WT CLC-2 (A), Tyr561Phe (B), or Tyr561Ala (C) exposed first to 140 (grey) and then 10 (blue) mM $[Cl^-]_o$ at pH_o = 7.3. Channels were activated using the voltage protocol shown in Fig. 4A.

A,B,C. Bottom panels: Voltage dependence of P_A (left), $P_{Glugate}$ (middle), and P_C (right) for WT CLC-2 (A), Tyr561Phe (B) and Tyr561Ala (C) determined first with 140 (grey) and then with 10 (blue) mM extracellular Cl^-. $[Cl^-]_i$ = 140 mM and $pH_i = pH_o$ = 7.3. Lines are fits of the data with Boltzmann equation. Voltage-dependent parameters $V_{0.5}$ and z are listed in Table 1.

To determine the conformational state of Glu_{gate} when Try561 is mutated, we analysed the pore structures of Tyr561Phe and Tyr561Ala mutants made *in-silico*. In contrast to the WT CLC-2 pores, the pore structures of Tyr561Phe and Tyr561Ala show a disordered Tyr561-H_2O-Glu_{gate} array in both pores (Supplementary Fig. 5). Although Glu_{gate} still interacted through H-bonds with the -NH groups of $_{466}AF_{467}$ and $_{212}KEG_{214}$, the Tyr561Phe-H_2O-Glu_{gate} bridge was formed only 16% of the time whereas the bridge Tyr561Ala-H_2O-Glu_{gate} was not formed at all. Hence, the Tyr561-H_2O-Glu_{gate} array is critical for maintaining the pore in a closed state.

The anomalous mole fraction behaviour of CLC-2 activation reveals the multi-ion occupancy of the pore.

MD simulations show that Cl^- can disrupt the Tyr561-H_2O-Glu_{gate} array and that Cl^- exit is facilitated when the pore is occupied by two Cl^- ions. These observations are in agreement with the idea that multi-ion occupancy(Hille, 2001) facilitates permeation by a knock-on mechanism(Khalili-Araghi et al., 2006; Kratochvil et al., 2016). To reveal the multi-ion occupancy of wild type CLC-2 channels we determine the anomalous mole fraction (AMF) behaviour using different acetate/Cl^- mole-fractions. As the acetate mole-fraction increased, we recorded less inward Cl^- currents and the depolarization-induced tail currents that saturated at less positive voltages (Fig. 6A). Increasing the acetate mole fraction shifted the voltage-dependent activation

curves first to the right and then to the left on the voltage axis (Fig. 6B). The corresponding $V_{0.5}$ values, when plotted against the acetate/Cl^- mole fractions, had a concave shape and peaked at 0.57 (Fig. 5D, black spheres). These data support the idea that multi-anion occupancy of the pore controls CLC-2 gating. If acetate and Cl^- occupy the pore then both anions contribute to the AMF dependence. To test this idea, we dialyzed the cells with acetate mole fractions that had the pH adjusted to 4.2 to protonate 79% of the acetate. Under this condition, we did not find evidence of AMF dependence in voltage activation (Fig. 6C). $V_{0.5}$ had a linear relationship with acetate/Cl^- mole-fractions (Fig. 6D, open circles), a behaviour similar to that observed with pure Cl^- solutions adjusted to pH 7.3 (Fig. 6D, green squares)(Sánchez-Rodríguez et al., 2010). This result also indicates that intracellular Cl^- but not intracellular H^+ control voltage activation.

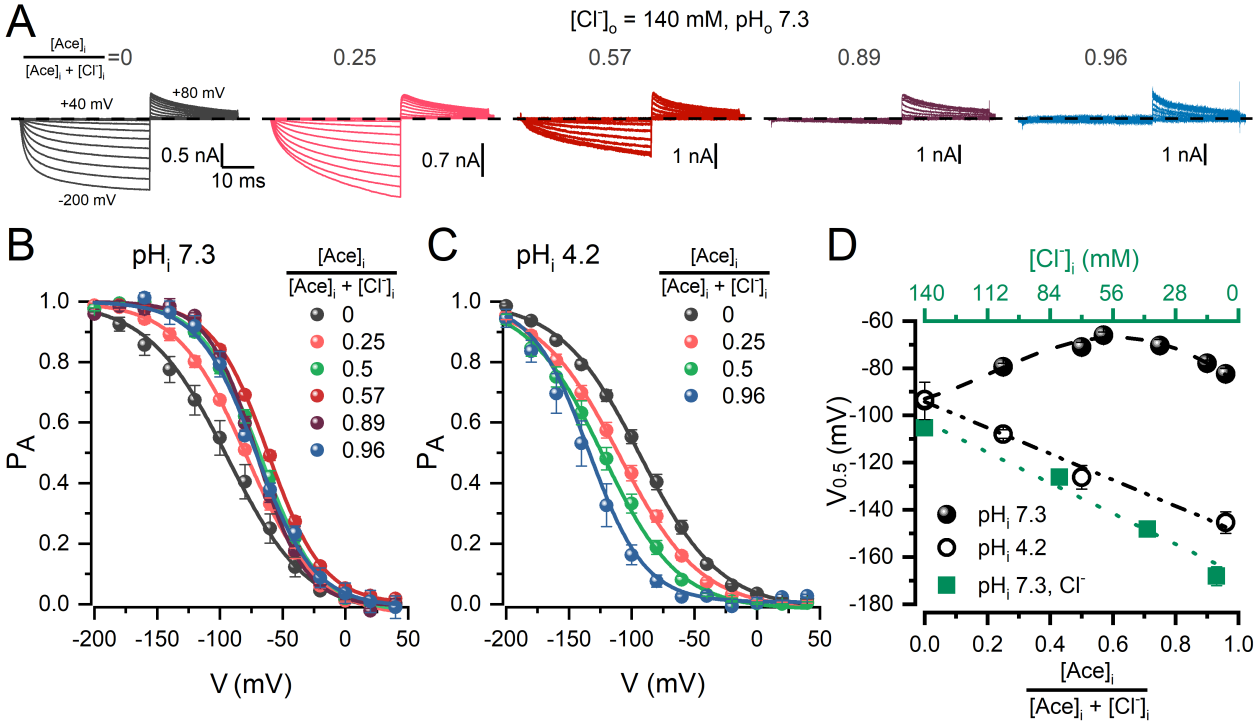

Fig. 6 Multi-ion pore occupancy regulates voltage-dependent activation.

A. Whole cell currents recorded from 5 different HEK cells expressing WT CLC-2 dialyzed with 0, 0.25, 0.57, 0.89, and 0.96 acetate mole fractions ($[Ace]_i/([Ace]_i+[Cl^-]_i)$). Currents were elicited by depolarization steps from -200 to +40 mV in increments of 20 mV. Tail currents were recorded at +80 mV. $[Cl^-]_o$ = 140 mM, $pH_e = pH_i$ = 7.3. Dash line indicates the 0 current level.

B,C. Voltage-dependent activation determined at pH_i of 7.3 (B) and 4.2 (C) using different acetate mole fractions. P_A was calculated using the tail current magnitude. The resulting curves were normalized to their respective tail current maximum obtained after fitting with the Boltzmann equation. Continuous lines are fits from which the voltage-dependent parameter $V_{0.5}$ and z were computed.

D. $V_{0.5}$ plotted against acetate mole fractions (circles) and $[Cl^-]_i$ (squares). Filled symbols correspond to data obtained at pH_i 7.3 whereas open symbols were collected at pH_i 4.2. $V_{0.5}$ values were obtained from Boltzmann fits to data shown in panels B and C. Similar data collected using intracellular solutions that contained unmixed Cl^- at pH_i = 7.3 was used to calculate $V_{0.5}$ (green squares).

Tyr561-H_2O-Glu_{gate} array inhibits Glu_{gate} protonation from the intracellular side.

A remarkable difference between CLC-0/CLC-1 and CLC-2 is their contrasting sensitivity to intracellular H^+. CLC-0 and CLC-1 require Glu_{gate} protonation for activation whereas CLC-2 does not(Rychkov et al., 1996; Sánchez-Rodríguez et al., 2012; Traverso et al., 2006b). The recent structure of hCLC-1 shows a bifurcation of the permeation pathway at the cytosolic side(Park and MacKinnon, 2018). For CLC exchangers this alternative pathway enables protonation of the

395 Glu_{gate} from the cytosolic side(Accardi et al., 2005). Our CLC-2 homology structures show the
396 presence of an uncoupled aqueous cavity at the same position as in CLC exchangers and hCLC-1
397 channels (Fig. 1C). Also, the homology model shows that Tyr561, Ile172, Phe269 and Thr520, all
398 hydrophobic residues, form a shield that faces the aqueous lacuna. We propose that these
399 residues form a hydrophobic gate that prevents pore bifurcation. The structures of Tyr561Phe
400 and Tyr561Ala shown in Figs. 7A and 7E, respectively, support this idea. The pore in Tyr561Phe
401 channels is occasionally bifurcated (Fig. 7A) but it becomes permanently bifurcated only in the
402 Tyr561Ala mutant (Fig. 7E). The bifurcation creates a forked water chain that exposes Glu_{gate} to
403 both the alternative and the canonical pathways. The hydrophobic gates of Tyr561Phe and
404 Tyr561Ala channels are shown in Figs. 7B and 7F, respectively, with yellow dashed lines
405 indicating the distance between paired residues. Fig. 7D shows distances between Phe269-
406 Tyr561 and Thr520-Ile172 in the two pores of WT CLC-2 and between Phe269-Tyr561Phe and
407 Thr520-Ile172 in the two pores of Tyr561Phe mutant channel. The distances remained around 3
408 Å and 6 Å, respectively, in both pairs, except for pore 2 in Phe269-Tyr561Phe which was about 6
409 Å. In contrast, the equivalent distances in both pores of the Tyr561Ala mutant increased to
410 around 5-11 Å (Fig. 7H). The consequence of these distortions in the hydrophobic gate was a
411 widening of the alternative pore radius with minimal effects on the canonical pore radius (Fig.
412 7C and 7G). The radius of the alternative pore in Tyr561Ala mutant became nearly identical to
413 the radius of the intracellular portion of the WT canonical pore (Fig. 1D). The alternative pore of
414 Tyr561Ala is wider than that of Tyr561Phe, which allowed the formation of the forked water
415 chain.

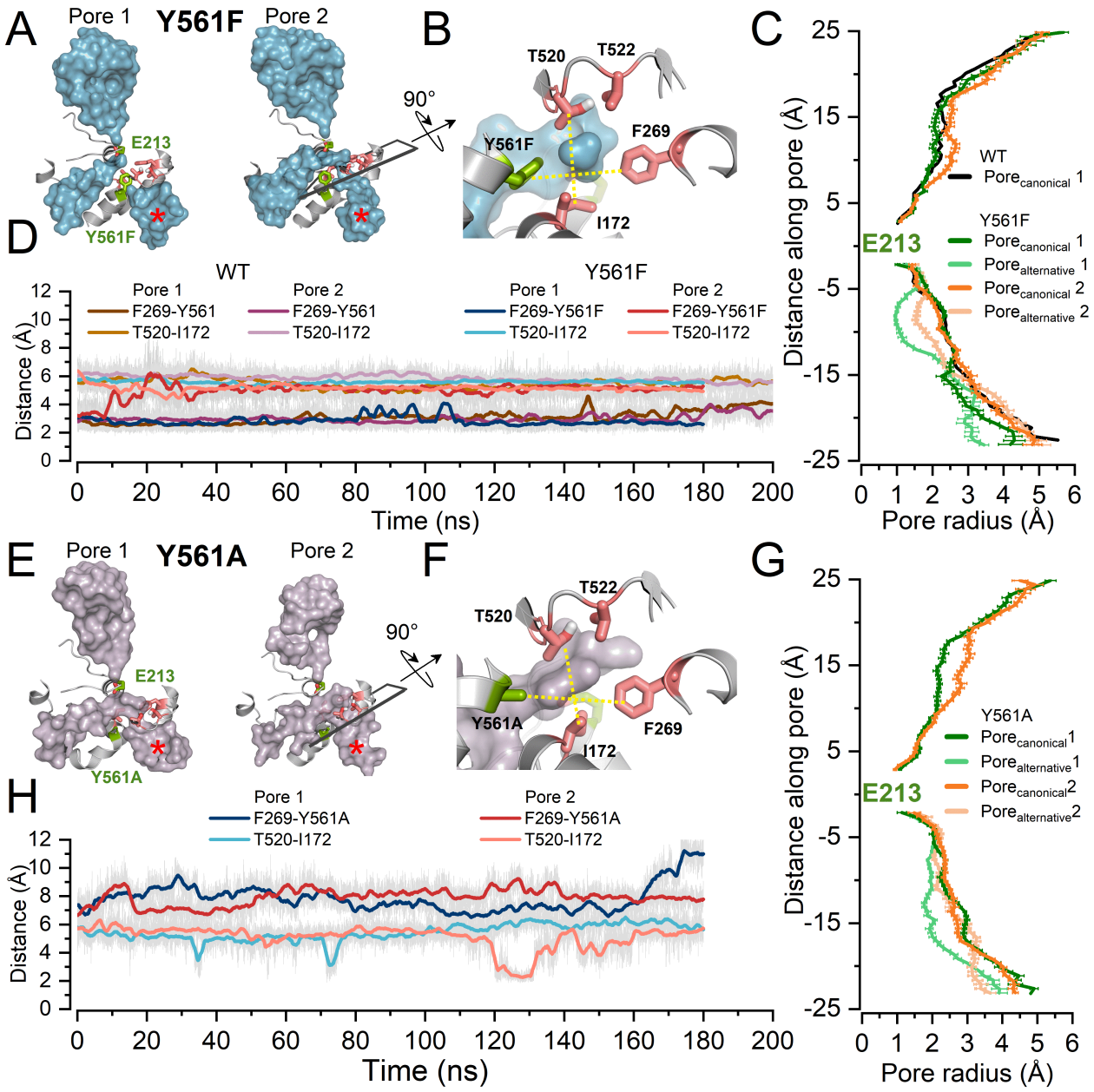

Fig. 7 The canonical pores of CLC-2 are uncoupled from an alternative pathway leading to the cytosol via a hydrophobic gate formed by Tyr561, Ile172, Phe269, and Thr520.

A,E. Canonical pores and the alternative pathways (indicated by red asterisks) are represented by the surface of water molecules in Tyr561Phe (A) and Tyr561Ala (E) mutants after 180 ns MD simulation at -500 mV. Residues Tyr561Phe, Tyr561Ala, and Glu_{gate} are

coloured in green. The tilted rectangles in pore 2 of both Tyr561Phe and Tyr561Ala mutants indicate the location plane for residues Ile172, Phe269, and Thr520 (pink) that comprise part of the hydrophobic gate.

B,F. Residues Ile172, Phe269, Thr520, Thr522, and Tyr561Phe (B) or Tyr561Ala (F) create a hydrophobic gate. Magnification of the planes delimited by black rectangles in A and E are rotated 90° to show the hydrophobic gate. The distances between residues connected by yellow dashed lines were measured to determine the size of the hydrophobic gate in Tyr561Phe (B) and Tyr561Ala (F) mutant channels.

D,H. Distances between residues of the hydrophobic gates in WT, Tyr561Phe, and Tyr561Ala channels as a function of the simulation time. Distances were measured diagonally between two pairs of residues: Phe269-Tyr561 and Thr520-Ile172 in WT, Phe269-Tyr561Phe and Thr520-Ile172 in the Tyr561Phe mutant (D) and between Phe269-Tyr561Ala and Thr520-Ile172 in the Tyr561Ala mutant (H). Measurements made at -500mV.

C,G. Average pore radius along canonical and alternative pores in WT and Tyr561Phe (C) and Tyr561Ala (G) mutants. The radius of both pores was measured and plotted for each channel. Canonical pores: 1 = black and dark green, 2 = dark orange; alternative pores: 1 = light green, 2 = light orange. The radius was measured at 0 mV during 30 ns every 1 ns. Note that the alternative pore is located after Glu_{gate}, between 0 and -25 Å.

We speculate that protonation of CLC-2 Glu_{gate} by intracellular H^+ is prevented(Sánchez-Rodríguez et al., 2012) by the hydrophobic gate that precludes pore bifurcation in WT CLC-2. To verify this we studied voltage-dependent activation at different intracellular pH (7.3, 5.5, and

443 4.3) in Tyr561Phe and Tyr561Ala mutants that have partially and fully bifurcated pores. Fig. 8
444 shows that both mutants were readily accessible to intracellular H^+. Tyr561Ala channels show
445 larger currents at positive potentials than Tyr561Phe channels upon intracellular acidification
446 (Figs. 8A and 8B). Relative to pH_i 5.5 the voltage dependence ($V_{0.5}$) of Tyr561Phe P_A (Fig 8A) at
447 pH_i 4.3 was reduced by 20 mV, whereas $V_{0.5}$ for Tyr561Ala (Fig. 8B) was reduced by 7 mV (Table
448 1). Notably, in Tyr561Ala the effects were readily measured at pH_i 5.5 and P_A increased from 0.2
449 to nearly 0.6 after decreasing pH_i from 7.3 to 4.3 (Fig. 8B). Similar effects were observed in the
450 voltage dependence of Glu_{gate} in mutants Tyr561Phe and Tyr561Ala (Figs. 8A and 8B). At pH_i 4.3,
451 Glu_{gate} of Tyr561Phe showed a reopening pattern at positive voltages whereas Glu_{gate} of
452 Tyr561Ala showed stronger activation at pH_i 5.5 and 4.3. At pH_i 4.3, $P_{Glugate}$ reached a minimum
453 value of about 0.7 indicating that Glu_{gate} remains nearly always open at this pH_i. Despite the
454 reopening at positive voltages induced by intracellular H^+, the $V_{0.5}$ of $P_{Glugate}$ was slightly altered
455 in both mutants at negative potentials (Table 1). Intracellular acidification also changed the
456 magnitude and voltage dependence of P_C. The $V_{0.5}$ value for Tyr561Phe was shifted by -42 mV at
457 pH_i 4.3 relative to pH_i 5.5, and by -10 mV for Tyr561Ala (Table 1).

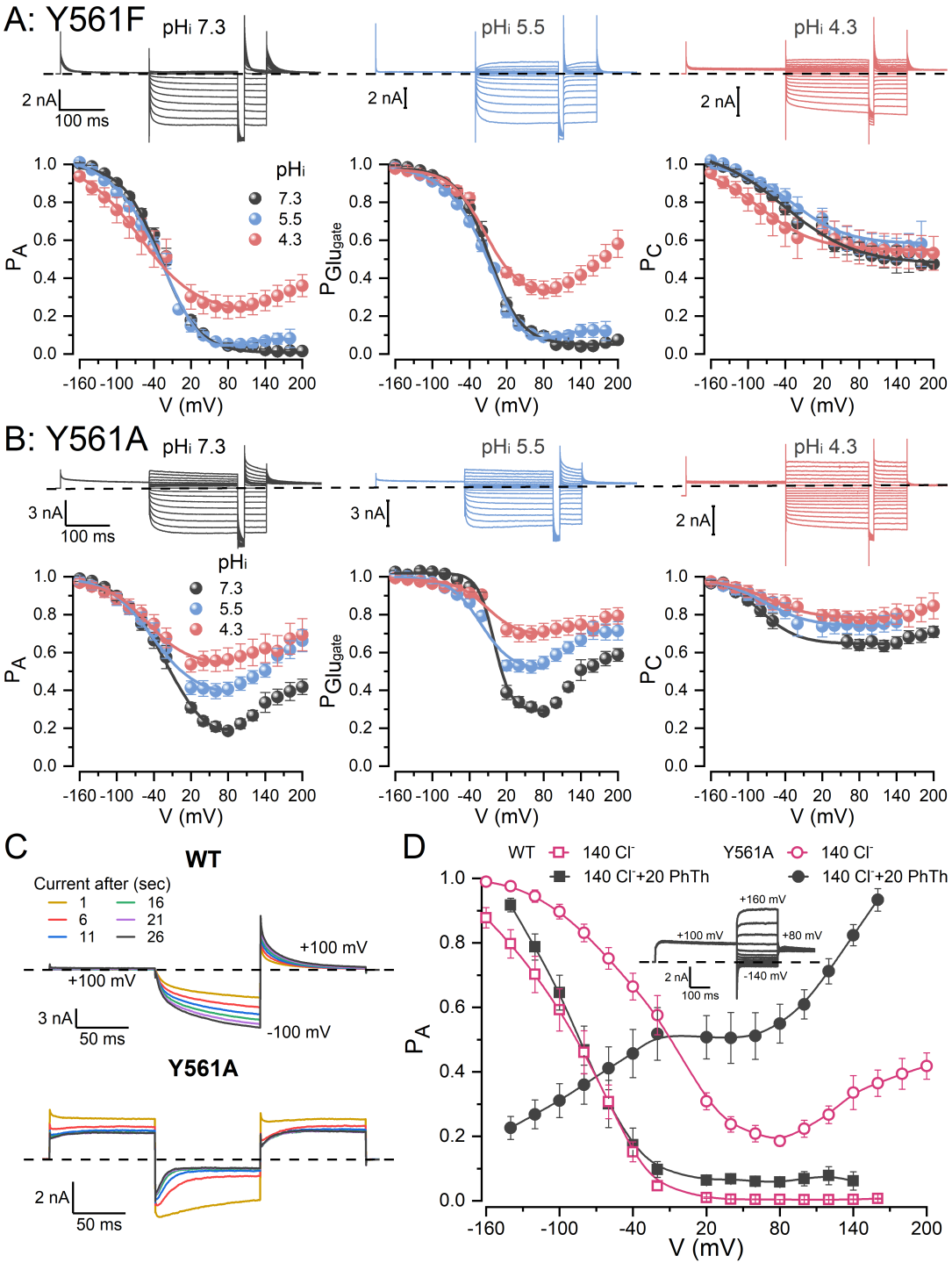

458

459 ***Fig. 8 Unrestrained Glu_{gate} renders CLC-2 sensitive to intracellular protons and phthalate.***

A,B. Top panels. Cl^- currents from 3 different HEK293 cells expressing the Tyr561Phe (A) or Tyr561Ala (B) mutants were recorded in the presence of 140 mM intracellular Cl^- and intracellular pH 7.3 (grey), 5.5 (blue), 4.3 (red). The voltage protocol showed in Fig. 4A was utilized in these experiments. Extracellular pH and $[Cl^-]_o$ were 7.3 and 140 mM, respectively.

A,B. Bottom panels. Voltage dependence of P_A, $P_{Glugate}$ and P_C for Tyr561Phe (A) and Tyr561Ala (B) are plotted using data collected at pH_i 7.3 (grey), 5.5 (blue) and 4.3 (red). Lines are fits of the data with the Boltzmann equation used to calculate $V_{0.5}$ and z parameters listed in Table 1.

C. 20 mM phthalate increases the whole cell current in WT CLC-2 (top panel) but inhibits the current in the Tyr561Ala (bottom panel) mutant channel. Whole cell currents were measured every 5 s after breaking the seal to get a pseudo-basal current.

D The inward rectification displayed by the WT and Tyr561Ala channels is inverted by phthalate in the Tyr561Ala channel. Comparison of the voltage-dependent activation curves determined for WT (squares) and Tyr561Ala (circles) in the absence (open) and presence (filled) of 20 mM phthalate. Phthalate was present in the intracellular solution. The inset shows whole cell recording from a cell expressing Tyr561Ala that was dialyzed with 20 mM phthalate.

Further evidence of a functional alternative pore was obtained by evaluating the effect of 20 mM phthalic acid at pH 7.3 applied to the intracellular side of WT and Tyr561Ala channels. Figure 8C shows that WT CLC-2 was not blocked by phthalic acid but Tyr561Ala mutant channels were. WT CLC-2 showed typical inwardly rectifying kinetics and the current increased during 26

s of recording. In contrast, the current through Tyr561Ala mutant was blocked as soon as the membrane was hyperpolarized and then unblocked at depolarized potential (Fig. 8C, lower panel). The voltage-dependent blockade by phthalate inverted the current rectification observed in Tyr561Ala (Insert in Fig. 8D). The current saturated at negative voltages and increased at a positive potential. Fig. 8D summarizes the voltage dependence of WT (squares) and Tyr561Ala (circles) channels in the absence (empty symbols) and presence (filled symbols) of 20 mM phthalic acid in the cytosolic side. Taken together, the structural data and the effects of intracellular H^+ and phthalate on WT and Tyr561Ala channels, indicate that the alternative pathway is not connected to the canonical pore in WT CLC-2 but it is connected in the Ty561Ala channel. These results explain the lack of protonation by intracellular H^+ in WT CLC-2 channels.

Discussion

The canonical pore stays closed by Tyr561-H_2O-Glu_{gate} and is opened by electro-steric repulsion.

The general features of the CLC proteins (TMD containing two pores, C-terminus with CB domains, and a curvilinear pore with a narrow constriction at Glu_{gate} location) are conserved in the equilibrated CLC-2 homology structure. However, there are important differences in specific regions associated with key functions. In CLC-2, Glu_{gate} is slightly bent towards the intracellular side making contact with Tyr561 via one H_2O molecule, a conformation apt for electro-steric repulsion with anions occupying the pore. This conformation of Glu_{gate} is analogous to that in the EcCLC and CmCLC Cl^-/H^+ exchangers but is different from the CLC-1 channel where Glu_{gate} is oriented off the pore lumen. At depolarized voltages, the pore of CLC-2 is a single empty

pathway closed by Tyr561-H_2O-Glu_{gate} whereas the pore of CLC-1 is an open bifurcated pathway occupied by two Cl^- ions(Park and MacKinnon, 2018). At hyperpolarized voltages, CLC-2 becomes open and occupied by two Cl^- ions. The closed/empty and open/occupied configurations at positive and negative voltages, respectively, correspond with CLC-2 function. Importantly, the canonical pores in CLC exchangers and CLC-1 channel are bifurcated but not in CLC-2 channel. In CLC Cl^-/H^+ exchangers, the alternative cavity includes Glu203 that is critical for Glu_{gate} protonation(Accardi et al., 2005), in CLC channels this residue is replaced by valine. In contrast, the pore of CLC-2 is isolated from the alternative cavity by hydrophobic residues that make a square-shaped hydrophobic gate. When we disrupted the hydrophobic gate, the pore became bifurcated and sensitive to intracellular H^+. We propose that a non-bifurcated pore or the absence of Glu residue or both explains why CLC-2 is insensitive to intracellular H^+. Tyr561 successfully shields CLC-2 from intracellular H^+.

Our data revealed that a two-leaf gate formed by the ionic interaction of Glu_{gate} with the -OH group of Tyr561 mediated by one polarized water molecule, works to close the canonical pore of CLC-2. Tyr561 is stiff and remains motionless during the entire gating process. Instead, Glu_{gate} is bound to Tyr561 in empty pores held at positive voltages but is released by Cl^- during activation. Free Glu_{gate} moves outwardly or inwardly depending on the electro-steric repulsive force generated by the Cl^- flux. Accordingly, mutating Tyr561 or Glu_{gate} leads to partially open (Tyr561Phe, Glu213Asp) or fully open (Tyr561Ala, Glu213A/V) phyenotypes(De Santiago et al., 2005; Niemeyer et al., 2003). We conclude that CLC-2 Glu_{gate} operates as a one-way check valve

similar to what has been proposed for K2P potassium channels(Schewe et al., 2016) and that Tyr561 prevents Glu_{gate} from opening in the inward direction.

Activation is possible by coupling gating to permeation.

Cl^- permeation was coupled to gating and lasted 580 ns (see video). During this time lapse, activation took place in five steps: the occupation of the pore by intracellular Cl^-, repulsion of Glu_{gate} by Cl^-, protonation of Glu_{gate}, double occupancy of the pore, and Cl^- exit (Fig. 9). During activation, major structural rearrangements occurred at the intracellular side, the gate and the extracellular side. At the intracellular side, loading and emptying S_i trigger a rapid interaction (8.3 ns) between the side chains of Lys568 and Glu174, similar to the opening/closing of a crab claw. At the extracellular side, a protonated Glu_{gate} stays far from Lys212, which allows the straightening and counter-clockwise bent of Lys212. This remarkably structural rearrangement allows Cl^- to interact with the Lys212 side chain during the exit process.

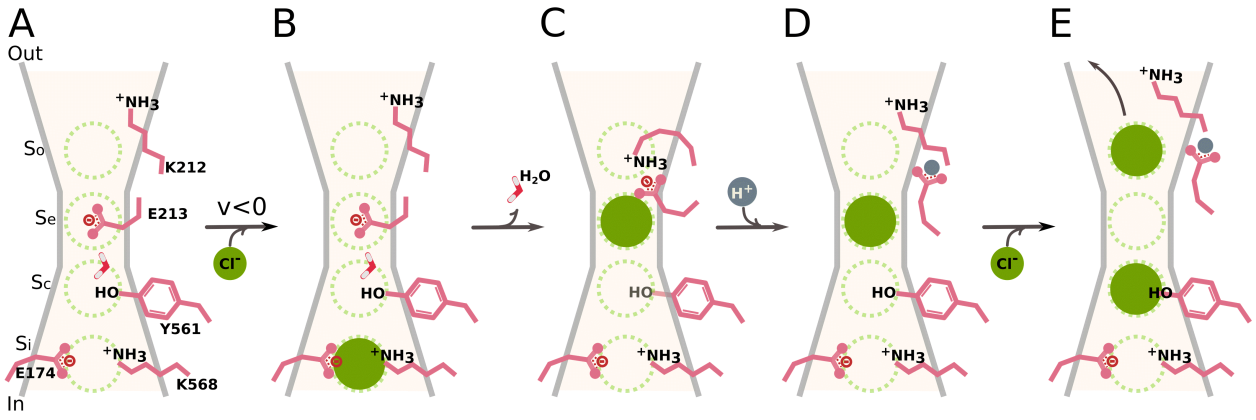

Fig. 9 Schematic representation of the electro-steric activation mechanism for CLC-2.

The Scheme depicts one pore, four anion-binding sites (S_i, S_C, S_e, and S_O), and the side chains of critical residues (Glu174, Lys568, Tyr561, Glu213, and Lys212) lining the pore. Regardless of

538 *voltage, the empty pore remains closed by the gate Tyr561-H_2O-Glu_{gate} (A). Upon a*
539 *hyperpolarization (V < 0), one intracellular Cl^- occupies S_i marking the beginning of the activation*
540 *process (B). The gate is split by electro-steric repulsion when Cl^- moves forward into the*
541 *permeation pathway and sits on S_C and S_e thus coupling permeation to gating (C). Then, Glu_{gate}*
542 *adopts an outward-facing conformation and interacts with Lys212, this conformation is*
543 *suggestive of a pre-open state (D). The Glu_{gate}-Lys212 salt-bridge is broken by protonation*
544 *allowing an outward straightening of the Lys212 side chain. Finally, Cl^- exits the pore when*
545 *another intracellular Cl^- occupies S_i and S_C (E). A doubly occupied pore indicates that the pore is*
546 *fully open and conductive.*

547 Despite that, the loaded Lys212 side chain was near to extracellular media, the Cl^- does not
548 readily escape because it sits in a deep well. For Cl^- to leave Lys212 another Cl^- ion needs to
549 occupy S_i. The doubly occupied pore condition (for 100 ns) is critical for initiating and
550 maintaining anion conduction (Fig. 9, video). A recent computational analysis aimed at
551 predicting intrinsic or extrinsic elements of a protein that could respond to changes in the local
552 electric field indicated that either Glu_{gate} or a Cl^- ion trapped in the pore could participate in
553 voltage sensing in CLC-1(Kasimova et al., 2018). According to our simulations, Glu_{gate} moved
554 outwardly ~7 Å from its original closed position but remained interacting with Lys212 until it
555 was protonated. A protonated Glu_{gate} do not contribute to voltage sensing. Instead, is the
556 negatively charged permeant Cl^- ion that goes across the entire electrical field that provides the
557 gating charge in CLC-2.

The gating mechanism proposed here differs substantially from the mechanism recently suggested by McKiernan et al,(McKiernan et al., 2020). These authors combined Markov state modelling with MD simulations and a homology structure of rat CLC-2 built using the CmCLC Cl^-/H^+ exchanger structure 3ORG as a template(Feng et al., 2010). They propose that entry of intracellular Cl^- requires rotation of the Ser168-Gly169-Ile170 backbone and opening of Glu_{gate} follows this in a Cl^--dependent manner. However, our results show that Lys568 and Glu174 are necessary for pore occupation by intracellular Cl^-. Another discrepancy is the role of Tyr561. McKiernan's work suggests that Tyr561 (Tyr559 in their homology structure) is irrelevant for CLC-2 gating, an idea supported by the lack of effect on single-channel conductance after mutating Tyr in CLC-0 and CLC-1 channels(Accardi and Pusch, 2003; Estévez et al., 2003; Ludewig et al., 1996). We observed that Glu_{gate} and Tyr561 remained in the same position regardless of voltage in empty pores. But, when a pore became occupied at a negative potential, Cl^- rapidly reconfigured the Tyr561-H_2O-Glu_{gate} array without disturbing Tyr561. These observations would suggest that Tyr561 does not play a role in gating. However, our MD simulations and electrophysiological data demonstrate that Tyr561 holds Glu_{gate} in the closed position and keeps intracellular protons from entering the pore. A limitation of McKiernan's data is that only one subunit was analysed at 0 mV, under these conditions the coupling of fast (Glu_{gate}) and common gates and the observation of gating transitions is limited because the open probability is almost null.

Is an electro-steric activation mechanism unique to CLC-2? We do not think so because voltage-dependent gating in CLC-0 and CLC-1 shows AMF behaviour, permeant anions facilitate gating,

and non-permeant anions support voltage-dependent gating of CLC-1(Chen, 2003; Chen and Miller, 1996; Pusch et al., 1995; Rychkov et al., 2001, 1998). However, pore bifurcation could be key in fine-tuning activation. Protonation of Glu_{gate} in the bifurcated pores of CLC-1 and CLC-0 could be facilitated *after* Glu_{gate} interacts with the permeant anions. Thus, it is likely that a mechanism entailing electro-steric gating is present in all CLC Cl^- channels. In addition to CLC Cl^- channels, the K2P K^+ channels that lack a voltage sensor domain also display voltage dependence due to the movement of K^+ ions along the pore(Kopec et al., 2019; Schewe et al., 2016). Similarly, the voltage-dependent gating of viral K^+ channel Kcv_{NTS} could rely on occupation by K^+ of an external site(Rauh et al., 2018). Interestingly, the outward movement of ions could explain the activation of PIEZO channels by voltage alone(Moroni et al., 2018). Thus, coupling ion permeation to pore gating through electro-steric repulsion might be a more general activation mechanism than previously estimated(Hilgemann, 2020).

Materials and Methods

Homology model of mouse CLC-2 and preparation of membrane-protein ensembles.

Initially, we constructed a model for the structure of the mouse CLC-2 Cl^- channel (908 aa) using the I-Tasser(Roy et al., 2010) server (https://zhanglab.ccmb.med.umich.edu/I-TASSER/) and the bovine CLC-K structure (5TQQ; Uniprot: E1B792; 687 aa) solved at 3.76 Å resolution using Cryo-EM(Park et al., 2017). This model structure was named CLC-$2^{CLC\text{-}K}$. mCLC-2 is 45.7% identical to CLC-K within the transmembrane region. However, the pores of mCLC-2 and CLC-K differ in two residues; valine replaces Glu_{gate} in CLC-K. We built an additional model using as template the hCLC-1 structure determined by Cryo-EM (6COY; UniProt: P35523; 988 aa)(Park and MacKinnon,

2018) and the Modeller v9.19 software(Sali and Blundell, 1993). This model was named CLC-2^{CLC-1}. The available hCLC-1 structure is based on 626 residues visible in the density maps. hCLC-1, a 988 residues long protein, was solved at 3.36 Å. CLC-2 and hCLC-1 are 56% identical within the transmembrane region and within the pore region, they differed by one amino acid. We measured the pore radius using CAVER 3.0(Chovancova et al., 2012).

The protonation state of ionisable residues at pH 7.3 was determined by PROPKA(Olsson et al., 2011). The protein, oriented using the Positioning of Proteins in Membrane server (PPM, http://opm.phar.umich.edu/server.php), was embedded in symmetric lipid bilayers of 1,2-dimyristoyl-sn-glycerol-3-phosphocholine (DMPC, CLC-2^{CLC-K}) or 1-palmitoyl-2-oleoyl-sn-glycerol-3-phosphocholine (POPC, CLC-2^{CLC-1}) generated using CHARMM-GUI(Jo et al., 2008) membrane builder (http://www.charmm-gui.org). The structures were solvated with water modelled by TIP3(Jorgensen et al., 1983) and 140 mM NaCl. Before MD simulation, the CLC-2^{CLC-K} and CLC-2^{CLC-1} systems consisted of 785 DMPC, 102741 TIP3, 800 Na^+ and 416 Cl^- contained in a 170 X 170 X 158 $Å^3$ simulation box, and of 554 POPC, 43283 TIP3, 110 Na^+, and 130 Cl^- contained in a 176 X 171 X 100 $Å^3$ box, respectively. Structures of Tyr561Phe and Tyr561Ala mutants were built on CLC-2^{CLC-1} using PyMol. Simulation boxes consisted of 554 POPC, 43271 TIP3, 111 Na^+, and 131 Cl^- in a 170 X 167 X 102 $Å^3$ box, and of 555 POPC, 43325 TIP3, 110 Na^+, and 130 Cl^- in a 170 X 165 X 102 $Å^3$ box for Tyr561Phe and Tyr561Ala, respectively.

Molecular dynamics simulations.

MD simulations were performed with the GPU-accelerated Gromacs 5.1 package(Berendsen et al., 1995) using the CHARMM36 force field(Klauda et al., 2010). The equations of motion were

621 solved using the leapfrog algorithm with a time step of 2fs. The temperature was coupled to the
622 Nosé−Hoover thermostat with a parameter τ_T = 0.2 ps at 300 K while the pressure was coupled
623 to the Parrinello−Rahman barostat(Parrinello and Rahman, 1981) with a coupling parameter τ_P =
624 0.5 ps at 1 atm. Bond distances were kept rigid by using the LINCS algorithm. The electrostatic
625 interactions were computed with the particle mesh Ewald (PME) approach(Darden et al., 1993)
626 with a tolerance of 10^{-6} for the real space contribution, with a grid spacing of 1.2 Å, spline
627 interpolation of order 4. In the isotropic NPT simulations, the real part of the Ewald summation
628 and the LJ interactions were truncated at 12 Å and 10 Å, respectively. Long-range corrections for
629 the LJ energy and pressure were included. All ensembles were minimized and equilibrated
630 during 100 and 30 ns (WT and mutants), before implementing a potential difference across the
631 membrane using the CompEl or the electric field protocols, respectively.

632 To perform CompEl we duplicated the CLC-2^{CLC-K} ensemble in the z-direction. Our CompEl
633 simulation box consisted of three compartments separated by two DMPC bilayers embedding
634 one CLC-2^{CLC-K} molecule each and solvated with 140 mM NaCl. Considering that charge (Δq),
635 membrane capacitance (C_m~1 μF/cm^2), and membrane voltage (V) are related by the equation
636 $V=\Delta q/C_m$, we unbalanced the charge between compartments by moving Na^+ ions to generate a
637 voltage gradient across the membranes(Kutzner et al., 2011). A difference of 2 or 20 Na^+ ions
638 between central and side compartments is equivalent to apply +94 or +940 mV and -94 or -940
639 mV to the intracellular sides of $^+$CLC-2^{CLC-K} (channel 1 inserted in bilayer 1) and of $^-$CLC-2^{CLC-K}
640 (channel 2 inserted in bilayer 2), respectively. This condition allowed us to analyse the CLC-2
641 closed state (positive voltages) and the open state (negative voltages) in the same MD

simulation. Additionally, we applied a uniform electric field of -500 mV perpendicular to the membrane (+z direction is from intracellular to extracellular side), Ez. The last 200 ns of the MD simulation of WT CLC-2^{CLC-K} (Ez= V/L = -3.16 mV/Å, where V is the voltage and L is the size to the box on z-direction) and on Tyr561Phe or Tyr561Ala mutants (Ez = -4.9 mV/Å for both) was ran using this protocol. A protonated $^{-}$CLC-2^{CLC-K} molecule was inserted in a DMPC bilayer and solvated with 140 mM NaCl. Thus, our hybrid protocol for MD simulation consisted of 480 ns CompEl (144 ns at ±94mV followed by 340 ns at ±940 mV), protonation of $^{-}$CLC-2^{CLC-K} Glu_{gate}, and of 200 ns applying an electric field of -500 mV to preserve the stability of the system. The protonation of Glu_{gate} ($Glu213^{H+}$, Fig. 3) was carried out using CHARMM-GUI and equilibrated for 10 ns before applying an electrical field.

Gromacs tools, VMD and PyMol were used for analysis and visualization.

Poisson-Boltzmann calculation

CLC-2^{CLC-K} in open and closed states was extracted at 565 ns from MD simulation. By solving the linearized Poisson-Boltzmann equation in CHARMM-GUI PBED solver(Im et al., 1998), the average electrostatic potential (EP) along the pore, identified by CAVER 3.0, was calculated on a 99 X 97 X 79 $Å^3$ (1 Å grid spacing), with the CHARMM36 force field. The average potential was calculated on the transversal area determined by the pore radius. The dielectric constant for protein was 1, for membrane and membrane head group was 2, and for solvent containing 150 mM salt concentration was 80. The thickness of the membrane was 35 Å. *In silico* mutants were generated with CHARMM-GUI tools.

Cell culture, transient expression and electrophysiological recordings

HEK-293 cells transfected with WT mouse ClC-2, mouse Tyr561Phe or mouse Tyr561Ala cDNAs were cultured and used for recording whole cell Cl^- currents (I_{Cl}) as previously described(De Jesús-Pérez et al., 2016; De Santiago et al., 2005; Sánchez-Rodríguez et al., 2012, 2010). Control solutions used to record I_{Cl} contained (in mM): TEA-Cl 139, $CaCl_2$ 0.5, HEPES 20 and D-mannitol 100 (external); and TEA-Cl 140, HEPES 20 and EGTA 20 (internal). HEPES was substituted by MES or phthalic acid to prepare solutions with low pH. The pH of these solutions was adjusted to 7.3 with TEA-OH. Average tonicity of external and internal solutions was 387.9±1.9 and 347.3±2.6 mosm/kg, respectively.

The mouse CLC-2 DNA inserted in the pGEM®-T vector was used for the heterologous expression in *Xenopus laevis* oocytes. The DNA was amplified, linearized with the Pme I enzyme (New England Biolabs, Inc., Ipswich, MA, USA) and transcribed in vitro using the T7 promoter mMESSAGE cRNA kit (Ambion, Austin, TX., USA). All mutations in this study were performed using standard PCR techniques and confirmed by sequencing the entire cassettes.

Procedures and methods involving *Xenopus laevis* frogs followed relevant guidelines and regulations as previously described(Rodríguez-Rangel et al., 2020). Briefly, oocytes contained in 1-3 mL of ovary lobes extracted via survival surgery were isolated by enzymatic digestion with collagenase type II (Worthington Biochemical Corp., NJ, USA) under mechanical agitation. After the isolation, each oocyte was injected with 40 ng of RNA encoding the WT mCLC-2 or mutants; oocytes were incubated for 2-7 days at 17 °C in a standard oocyte saline solution containing (in mM): 100 NaCl, 1 $MgCl_2$, 10 HEPES, 2 KCl and 1.8 $CaCl_2$ with 50 µg/mL gentamycin at pH 7.5. All

683 chemical compounds utilized for this study were purchased from Sigma-Aldrich (Sigma-Aldrich
684 Co., St. Louis, MO, USA).

685 I_{Cl} from HEK cells was recorded using a protocol that consisted of holding the cell at 0 mV, then
686 applying a voltage between +60 or +200 to -200 mV in 20 mV steps and then returning the cell
687 to +60 or +80 mV. All experiments were performed at room temperature (21-23^{o}C). To
688 determine the effect of AMF on ClC-2 activation, we used internal solutions containing 0.0, 0.25,
689 0.5, 0.75, and 1.0 acetate mole fractions. I_{Cl} was recorded using pClamp 10 and sampling at 500
690 kHz. Otherwise, currents were sampled using pClamp V8. To avoid electrode polarization while
691 using internal solutions with low Cl^- we used an electrode embedded in a 3 M KCl/3% agar
692 jacket(Shao and Feldman, 2007). Membrane and reversal potentials were corrected off-line
693 using liquid junction potentials experimentally measured(Neher, 1992).

694 Electrophysiology measurements in *Xenopus laevis* oocytes were conducted using the cut-open
695 oocyte voltage clamp methodology(Siefani and Bezanilla, 1998). The internal recording solution
696 contained (in mM): 136 NMDG (N-methyl-D-glucamine)-HCl, 2 $MgCl_2$, 10 EGTA, 10 HEPES. The
697 external recording solution was composed (in mM) by 130 NMDG-HCl, 4 $MgCl_2$, 1 $BaCl_2$ and 10
698 HEPES. Both solutions were adjusted to pH 7.3 with 1M NMDG. I_{Cl} was amplified and digitized
699 using the Oocyte Clamp Amplifier CA-1A (Dagan Corporation, Minneapolis, MN, USA) and the
700 USB-1604-HS-2AO Multifunction Card (Measurement Computing, Norton, MA, USA). The
701 acquisition system was controlled by the GpatchMC64 program (Department of Anesthesiology,
702 UCLA, Los Angeles, CA, USA) via a personal computer. Recordings sampled at 100 kHz and
703 filtered at 10 kHz were obtained at room temperature (21–23 °C).

Analysis

The voltage dependence of the open probability (P_A) was determined by constructing curves of P_A (=G/G_{max}) versus voltage ($P_A(V)$). Conductance (G) at each V was calculated as $I_{Cl}/(V-V_r)$, where V is the membrane potential and V_r is the reversal potential. The maximum conductance (G_{max}) was estimated before normalization by fitting the G against V curves with the Boltzmann equation:

$$\frac{G}{G_{max}} = \frac{1}{1+e^{-\frac{zF}{RT}(V-V_{0.5})}} \qquad \text{Equation 1}$$

where z is the apparent charge, F is the Faraday constant, R is the gas constant, T is the temperature and $V_{0.5}$ is the V needed to reach P_A = 1/2. Instantaneous current-voltage plots were constructed using the magnitude of tail currents recorded at different V and fitted to a linear function to determine V_r.

The voltage-dependence of the open probability of Glu_{gate} ($P_{GluGate}$)and common (P_C) gates was calculated as described before(De Santiago et al., 2005). Briefly, we used a 15 ms hyperpolarization pulse to -200 mV to completely open Glu_{gate} (time constant ≤3ms) so $P_{Glugate}$ ~1. When I_{Cl} reaches steady-state $P_A = P_{Glugate} * P_C$, before the hyperpolarization step to -200 mV I_{Cl} obeys the relationship $I_o = 2NiP_{Glugate}*P_C$, and after the hyperpolarization step I_{Cl} is given by $I_{ahs} \approx 2NiP_C$. Here, N is the total number of channels, i is the single-channel current, all multiplied by 2 because is a two-pore channel. Hence, $P_{Glugate}$ can be calculated as I_o/I_{ahs} and $P_C = P_A/P_{Glugate}$.

Cut open voltage-clamp recordings were included in the analysis after determining that the reversal potential values of I_{Cl} were near the predicted Nernst potential for Cl^-. I_{Cl} recordings

724 were analysed with the software Analysis (Department of Anesthesiology, UCLA, Los Angeles,
725 CA, USA).

726 Figures and fits were carried out using Origin (Origin Lab, Northampton, MA). Experimental data
727 are plotted as mean ± SEM of n (number of independent experiments). Dashed black lines in
728 each Figure indicate I_{Cl} = 0. Where necessary, a paired Student t-test was used to evaluate
729 significant differences at $P<0.05$ between data sets.

730 **ACKNOWLEDGEMENTS**

731 The authors thank Dr Patricia Perez-Cornejo for critical comments, Carmen Y. Hernandez-
732 Carballo for technical assistance. The work was supported by grants 219949 and FC-2016-01-
733 1955 from CONACyT, Mexico. RG-G is a recipient of a Graduate Student Fellowship #726278
734 from CONACyT, Mexico. JJDeJ-P was supported by a Graduate Student Fellowship and
735 Postdoctoral Fellowship 234820 and 711128 from CONACyT, Mexico, respectively.

736 **AUTHOR CONTRIBUTIONS**

737	JJDeJP	Designed research, performed patch-clamp experiments, performed MD
738		simulations, analysed data and wrote the manuscript.
739	VDRJ	Performed patch-clamp experiments, analysed data and review the
740		manuscript.
741	ILGH	Performed patch-clamp experiments
742	GAMM	Performed MD simulations and analysed the data

743	JESR, RG-G	Performed electrophysiological experiments in X. oocytes, analysed the
744		data and wrote the manuscript.
745	JA	Designed research, analysed data, wrote the paper, and secure funds.

746 **COMPETING INTEREST**

747 The authors declare no competing interests

748 **REFERENCES**

749 Accardi A, Pusch M. 2003. Conformational changes in the pore of CLC-0. *J Gen Physiol* **122**:277–
750 293. doi:10.1085/jgp.200308834

751 Accardi A, Walden M, Nguitragool W, Jayaram H, Williams C, Miller C. 2005. Separate Ion
752 Pathways in a Cl- /H+ Exchanger. *J Gen Physiol* **126**:563–570. doi:10.1085/jgp.200509417

753 Allouche A. 2012. Software News and Updates Gabedit — A Graphical User Interface for
754 Computational Chemistry Softwares. *J Comput Chem* **32**:174–182. doi:10.1002/jcc

755 Berendsen HJC, van der Spoel D, van Drunen R. 1995. GROMACS: A message-passing parallel
756 molecular dynamics implementation. *Comput Phys Commun* **91**:43–56. doi:10.1016/0010-
757 4655(95)00042-E

758 Bezanilla F. 2008. How membrane proteins sense voltage. *Nat Rev Mol Cell Biol* **9**:323–332.
759 doi:10.1038/nrm2376

760 Bezanilla F. 2002. Voltage sensor movements. *J Gen Physiol*. doi:10.1085/jgp.20028660

761 Boccaccio A, Pusch M, Boccaccio A, Pusch M. 2018. TMEM16 Ca2+ Activated Cl– Channels and

762 CLC Chloride Channels and TransportersThe Oxford Handbook of Neuronal Ion Channels.
763 Oxford University Press. doi:10.1093/oxfordhb/9780190669164.013.17

764 Chen T-Y. 2003. Coupling gating with ion permeation in ClC channels. *Sci STKE* **2003**:pe23.
765 doi:10.1126/stke.2003.188.pe23

766 Chen TY, Miller C. 1996. Nonequilibrium gating and voltage dependence of the ClC-0 Cl-
767 channel. *J Gen Physiol* **108**:237–250. doi:10.1085/jgp.108.4.237

768 Chovancova E, Pavelka A, Benes P, Strnad O, Brezovsky J, Kozlikova B, Gora A, Sustr V, Klvana M,
769 Medek P, Biedermannova L, Sochor J, Damborsky J. 2012. CAVER 3.0: A Tool for the
770 Analysis of Transport Pathways in Dynamic Protein Structures. *PLoS Comput Biol* **8**:23–30.
771 doi:10.1371/journal.pcbi.1002708

772 Cox CD, Bavi N, Martinac B. 2016. Origin of the Force: The Force-From-Lipids Principle Applied to
773 Piezo Channels. doi:10.1016/bs.ctm.2016.09.001

774 Crozier PS, Henderson D, Rowley RL, Busath DD. 2001. Model channel ion currents in NaCl-
775 extended simple point charge water solution with applied-field molecular dynamics.
776 *Biophys J*. doi:10.1016/S0006-3495(01)75946-2

777 Darden T, York D, Pedersen L. 1993. Particle mesh Ewald: An N·log(N) method for Ewald sums in
778 large systems. *J Chem Phys* **98**:10089–10092. doi:10.1063/1.464397

779 De Jesús-Pérez JJ, Castro-Chong A, Shieh RC, Hernández-Carballo CY, De Santiago-Castillo JA,
780 Arreola J. 2016. Gating the glutamate gate of CLC-2 chloride channel by pore occupancy. *J*
781 *Gen Physiol* **147**:25–37. doi:10.1085/jgp.201511424

De Santiago JA, Nehrke K, Arreola J. 2005. Quantitative analysis of the voltage-dependent gating of mouse parotid ClC-2 chloride channel. *J Gen Physiol* **126**:591–603. doi:10.1085/jgp.200509310

Dutzler R, Campbel EB, Cadene M, Chait BT, MacKinnon R. 2002. X-ray structure of a ClC chloride channel at 3.0A reveals the molecular basis of anion selectivity. *Nature* **415**:287–294.

Dutzler R, Campbell EB, MacKinnon R. 2003. Gating the selectivity filter in ClC chloride channels. *Science* **300**:108–112. doi:10.1126/science.1082708

Estévez R, Schroeder BC, Accardi A, Jentsch TJ, Pusch M. 2003. Conservation of chloride channel structure revealed by an inhibitor binding site in ClC-1. *Neuron* **38**:47–59. doi:10.1016/S0896-6273(03)00168-5

Feng L, Campbell EB, Hsiung Y, MacKinnon R. 2010. Structure of a eukaryotic CLC transporter defines an intermediate state in the transport cycle. *Science* **330**:635–41. doi:10.1126/science.1195230

Goldschen-Ohm MP, Chanda B. 2017. SnapShot: Channel Gating Mechanisms. *Cell* **170**:594-594.e1. doi:10.1016/j.cell.2017.07.019

Hilgemann DW. 2020. Regulation of ion transport from within ion transit pathways. *J Gen Physiol* **152**. doi:10.1085/jgp.201912455

Hille B. 2001. Ion Channels of Excitable Membranes, Third Edit. ed. Sinauer Associates Is an Imprint of Oxford University Press.

802 Hille B, Armstrong CM, MacKinnon R. 1999. Ion channels: From idea to reality. *Nat Med*.
803 doi:10.1038/13415

804 Im W, Beglov D, Roux B. 1998. Continuum solvation model: Computation of electrostatic forces
805 from numerical solutions to the Poisson-Boltzmann equation. *Comput Phys Commun*.
806 doi:10.1016/s0010-4655(98)00016-2

807 Jentsch TJ, Pusch M. 2018. CLC chloride channels and transporters: Structure, function,
808 physiology, and disease. *Physiol Rev*. doi:10.1152/physrev.00047.2017

809 Jiang Y, Ruta V, Chen J, Lee A, Mackinnon R. 2003. The principle of gating charge movement in a
810 voltage-dependent K+ channel **423**:42–48.

811 Jo S, Kim T, Iyer VG, Im W. 2008. CHARMM-GUI: A web-based graphical user interface for
812 CHARMM. *J Comput Chem*. doi:10.1002/jcc.20945

813 Jorgensen WL, Chandrasekhar J, Madura JD, Impey RW, Klein ML. 1983. Comparison of simple
814 potential functions for simulating liquid water. *J Chem Phys* **79**:926–935.
815 doi:10.1063/1.445869

816 Kasimova MA, Lindahl E, Delemotte L. 2018. Determining the molecular basis of voltage
817 sensitivity in membrane proteins. *J Gen Physiol* **215**:1444–1458.
818 doi:10.1085/jgp.201812086

819 Khalili-Araghi F, Tajkhorshid E, Schulten K. 2006. Dynamics of K+ ion conduction through Kv1.2.
820 *Biophys J*. doi:10.1529/biophysj.106.091926

Klauda JB, Venable RM, Freites JA, O'Connor JW, Tobias DJ, Mondragon-Ramirez C, Vorobyov I, MacKerell AD, Pastor RW. 2010. Update of the CHARMM All-Atom Additive Force Field for Lipids: Validation on Six Lipid Types. *J Phys Chem B*. doi:10.1021/jp101759q

Kopec W, Rothberg BS, de Groot BL. 2019. Molecular mechanism of a potassium channel gating through activation gate-selectivity filter coupling. *Nat Commun* **10**. doi:10.1038/s41467-019-13227-w

Kratochvil HT, Carr JK, Matulef K, Annen AW, Li H, Maj M, Ostmeyer J, Serrano AL, Raghuraman H, Moran SD, Skinner JL, Perozo E, Roux B, Valiyaveetil FI, Zanni MT. 2016. Instantaneous ion configurations in the K+ion channel selectivity filter revealed by 2D IR spectroscopy. *Science (80-)*. doi:10.1126/science.aag1447

Kutzner C, Grubmüller H, De Groot BL, Zachariae U. 2011. Computational electrophysiology: The molecular dynamics of ion channel permeation and selectivity in atomistic detail. *Biophys J* **101**:809–817. doi:10.1016/j.bpj.2011.06.010

Long SB, Campbell EB, MacKinnon R. 2005. Voltage sensor of Kv1.2: Structural basis of electromechanical coupling. *Science (80-)*. doi:10.1126/science.1116270

Ludewig U, Pusch M, Jentsch TJ. 1996. Two physically distinct pores in the dimeric CIC-0 chloride channel. *Nature*. doi:10.1038/383340a0

McKiernan KA, Koster AK, Maduke M, Pande VS. 2020. Dynamical model of the CLC-2 ion channel reveals conformational changes associated with selectivity-filter gating. *PLoS Comput Biol*. doi:10.1371/journal.pcbi.1007530

841 Miller C. 2006. ClC chloride channels viewed through a transporter lens. *Nature* **440**:484–9.
842 doi:10.1038/nature04713

843 Moroni M, Servin-Vences MR, Fleischer R, Sánchez-Carranza O, Lewin GR. 2018. Voltage gating
844 of mechanosensitive PIEZO channels. *Nat Commun* **9**. doi:10.1038/s41467-018-03502-7

845 Neher E. 1992. Correction for liquid junction potentials in patch clamp experiments. *Methods*
846 *Enzymol*. doi:10.1016/0076-6879(92)07008-C

847 Niemeyer MI, Cid LP, Yusef YR, Briones R, Sepúlveda F V. 2009a. Voltage-dependent and -
848 independent titration of specific residues accounts for complex gating of a ClC chloride
849 channel by extracellular protons. *J Physiol* **587**:1387–400.
850 doi:10.1113/jphysiol.2008.167353

851 Niemeyer MI, Cid LP, Yusef YR, Briones R, Sepúlveda F V. 2009b. Voltage-dependent and -
852 independent titration of specific residues accounts for complex gating of a ClC chloride
853 channel by extracellular protons. *J Physiol*. doi:10.1113/jphysiol.2008.167353

854 Niemeyer MI, Cid LP, Zúñiga L, Catalán M, Sepúlveda F V. 2003. A conserved pore-lining
855 glutamate as a voltage- and chloride-dependent gate in the ClC-2 chloride channel. *J*
856 *Physiol* **553**:873–9. doi:10.1113/jphysiol.2003.055988

857 Olsson MHM, SØndergaard CR, Rostkowski M, Jensen JH. 2011. PROPKA3: Consistent treatment
858 of internal and surface residues in empirical p K a predictions. *J Chem Theory Comput*.
859 doi:10.1021/ct100578z

860 Park E, Campbell EB, MacKinnon R. 2017. Structure of a CLC chloride ion channel by cryo-

electron microscopy. *Nature* **541**:500–505. doi:10.1038/nature20812

Park E, MacKinnon R. 2018. Structure of the CLC-1 chloride channel from Homo sapiens. *Elife* **7**. doi:10.7554/eLife.36629

Parrinello M, Rahman A. 1981. Polymorphic transitions in single crystals: A new molecular dynamics method. *J Appl Phys* **52**:7182–7190. doi:10.1063/1.328693

Pusch M, Ludewig U, Rehfeldt A, Jentsch TJ. 1995. Gating of the voltage-dependent chloride channel CIC-0 by the permeant anion. *Nature*. doi:10.1038/373527a0

Rauh O, Hansen UP, Scheub DD, Thiel G, Schroeder I. 2018. Site-specific ion occupation in the selectivity filter causes voltage-dependent gating in a viral K+ channel. *Sci Rep* **8**:1–15. doi:10.1038/s41598-018-28751-w

Rodríguez-Rangel S, Bravin AD, Ramos-Torres KM, Brugarolas P, Sánchez-Rodríguez JE. 2020. Structure-activity relationship studies of four novel 4-aminopyridine K+ channel blockers. *Sci Rep*. doi:10.1038/s41598-019-56245-w

Roux B. 2008. The membrane potential and its representation by a constant electric field in computer simulations. *Biophys J*. doi:10.1529/biophysj.108.136499

Roy A, Kucukural A, Zhang Y. 2010. I-TASSER: A unified platform for automated protein structure and function prediction. *Nat Protoc* **5**:725–738. doi:10.1038/nprot.2010.5

Rychkov GY, Pusch M, Astill DS, Roberts ML, Jentsch TJ, Bretag AH. 1996. Concentration and pH dependence of skeletal muscle chloride channel ClC-1. *J Physiol* **497 (Pt 2**:423–435.

Rychkov GY, Pusch M, Roberts ML, Bretag AH. 2001. Interaction of hydrophobic anions with the rat skeletal muscle chloride channel ClC-1: Effects on permeation and gating. *J Physiol* **530**:379–393. doi:10.1111/j.1469-7793.2001.0379k.x

Rychkov GY, Pusch M, Roberts ML, Jentsch TJ, Bretag a H. 1998. Permeation and block of the skeletal muscle chloride channel, ClC-1, by foreign anions. *J Gen Physiol* **111**:653–65. doi:10.1085/jgp.111.5.653

Sali A, Blundell TL. 1993. Comparative protein modelling by satisfaction of spatial restraints. *J Mol Biol* **234**:779–815.

Sánchez-Rodríguez JE, De Santiago-Castillo JA, Arreola J. 2010. Permeant anions contribute to voltage dependence of ClC-2 chloride channel by interacting with the protopore gate. *J Physiol* **588**:2545–2556. doi:10.1113/jphysiol.2010.189175

Sánchez-Rodríguez JE, De Santiago-Castillo JA, Contreras-Vite JA, Nieto-Delgado PG, Castro-Chong A, Arreola J. 2012. Sequential interaction of chloride and proton ions with the fast gate steer the voltage-dependent gating in ClC-2 chloride channels. *J Physiol* **590**:4239–4253. doi:10.1113/jphysiol.2012.232660

Schewe M, Nematian-Ardestani E, Sun H, Musinszki M, Cordeiro S, Bucci G, De Groot BL, Tucker SJ, Rapedius M, Baukrowitz T. 2016. A Non-canonical Voltage-Sensing Mechanism Controls Gating in K2P K+ Channels. *Cell* **164**:937–949. doi:10.1016/j.cell.2016.02.002

Shao XM, Feldman JL. 2007. Micro-agar salt bridge in patch-clamp electrode holder stabilizes electrode potentials. *J Neurosci Methods* **159**:108–115.

doi:10.1016/j.jneumeth.2006.07.001

Siefani E, Bezanilla F. 1998. Cut-open oocyte voltage-clamp technique. *Methods Enzymol*. doi:10.1016/S0076-6879(98)93020-8

Thiemann A, Gründer S, Pusch M, Jentsch TJ. 1992. A chloride channel widely expressed in epithelial and non-epithelial cells. *Nature*. doi:10.1038/356057a0

Traverso S, Zifarelli G, Aiello R, Pusch M. 2006a. Proton sensing of CLC-0 mutant E166D. *J Gen Physiol* **127**:51–65. doi:10.1085/jgp.200509340

Traverso S, Zifarelli G, Aiello R, Pusch M. 2006b. Proton sensing of CLC-0 mutant E166D. *J Gen Physiol* **127**:51–65. doi:10.1085/jgp.200509340